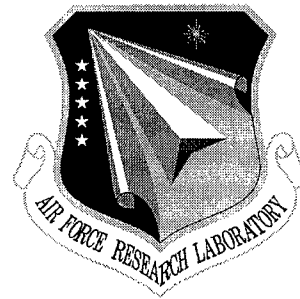AFRL-SN-RS-TR-1998-228
Interim Technical Report
January 1999

MULTICHANNEL RECEIVER CHARACTERIZATION FOR ADAPTIVE ARRAY APPLICATIONS -
Phase 4: Calibration Procedures/Tests

W. L. Simkins, Proprietor

APPROVED FOR PUBLIC RELEASE; DISTRIBUTION UNLIMITED.

19990209 106

AIR FORCE RESEARCH LABORATORY
SENSORS DIRECTORATE
ROME RESEARCH SITE
ROME, NEW YORK

This report has been reviewed by the Air Force Research Laboratory, Information Directorate, Public Affairs Office (IFOIPA) and is releasable to the National Technical Information Service (NTIS). At NTIS it will be releasable to the general public, including foreign nations.

AFRL-SN-RS-TR-1998-228 has been reviewed and is approved for publication.

APPROVED:

ELAINE KORDYBAN
Project Engineer

FOR THE DIRECTOR:

ROBERT G. POLCE, Acting Chief
Rome Operations Office
Sensors Directorate

REPORT DOCUMENTATION PAGE

1. AGENCY USE ONLY (Leave blank)	2. REPORT DATE	3. REPORT TYPE AND DATES COVERED
	January 1999	Interim Jan 97 - Sep 97

4. TITLE AND SUBTITLE
MULTICHANNEL RECEIVER CHARACTERIZATION FOR ADAPTIVE ARRAY APPLICATIONS - Phase 4: Calibration Procedures/Tests

5. FUNDING NUMBERS
C - F30602-95-C-0015
PE - 62702F
PR - 4506
TA - SN
WU - IS

6. AUTHOR(S)

William L. Simkins

7. PERFORMING ORGANIZATION NAME(S) AND ADDRESS(ES)
William L. Simkins, Proprietor
2600 Waldron Road
Camden NY 13316

8. PERFORMING ORGANIZATION REPORT NUMBER

N/A

9. SPONSORING/MONITORING AGENCY NAME(S) AND ADDRESS(ES)

Air Force Research Laboratory/SNRD
26 Electronic Parkway
Rome NY 13441-4514

10. SPONSORING/MONITORING AGENCY REPORT NUMBER

AFRL-SN-RS-TR-1998-228

11. SUPPLEMENTARY NOTES

Air Force Research Laboratory Engineer: Elaine Kordyban/SNRD/(315) 330-4481

12a. DISTRIBUTION AVAILABILITY STATEMENT

Approved for public release; distribution unlimited.

12b. DISTRIBUTION CODE

13. ABSTRACT (Maximum 200 words)

This report described Phase 4 of a multi-phase effort to develop an existing multichannel receiver into a multi-use bistatic testbed. It presents procedures developed for using the calibrated transponder in the radar cross section measurements of clutter and targets and using these procedures in the measurement of the local clutter environment.

14. SUBJECT TERMS

Surveillance, Bistatic Radar, Radar Cross Section, Terrain Clutter

15. NUMBER OF PAGES
98

16. PRICE CODE

17. SECURITY CLASSIFICATION OF REPORT	18. SECURITY CLASSIFICATION OF THIS PAGE	19. SECURITY CLASSIFICATION OF ABSTRACT	20. LIMITATION OF ABSTRACT
UNCLASSIFIED	UNCLASSIFIED	UNCLASSIFIED	UL

TABLE OF CONTENTS

LIST OF FIGURES

LIST OF TABLES

1.0 INTRODUCTION

The Department of Defense has an interest in the detection of low visibility threats. One approach, currently under investigation by the Air Force Research Laboratory (AFRL), involves the development of Advanced Offboard Bistatic Technology for improved detection and tracking of low visibility targets. For the purpose of this report, low visibility targets are those with an inherently low radar cross section (RCS) or those that use natural features to reduce or mask the targets return. Stealth technology is an example of the first type while the aircraft using terrain shadowing or vehicles using the attenuation and clutter of a vegetation canopy are examples of the second type. The sensor technology involves the development of a modern adaptive multichannel bistatic radar system for use with cooperative and non-cooperative transmitters.

A goal of an adaptive ground-based or airborne surveillance radar system is to have optimum or near-optimum detection and tracking of weak targets in the presence of strong clutter and interference while maintaining a low false alarm rate. Several adaptive techniques have been suggested to meet these criteria including adaptive space-time processing [1,2], adaptive multipath and jamming cancellation [3,4] and adaptive beamforming [5]. The performance of all these techniques depends on the target-to-noise ratios (T/N), the clutter-plus-interference-to-noise ratios (C+I/N) and the spatial-temporal amplitude and correlation statistics of the target, the clutter and the interference. Radar measurements and experiments are required to demonstrate the performance of these techniques and to quantify the target and clutter statistics that determined each technique's limitations. The objective of this effort is to assist Rome Laboratory in creating a fundamental multichannel measurement capability to perform multidomain adaptive radar experiments.

W. L. Simkins is performing a multi-phase effort to assist the AFRL in the development of the existing multichannel receiver into a multi-use bistatic testbed. The first phase report [6] provided an evaluation of the existing system with recommendations for improving performance. The second phase recommended the procedures and post-A/D algorithms for maintaining real-time calibration of the adaptive array receiver [7]. The third task presented an assessment of the existing adaptive array receiver's utility for investigating clutter phenomenology and defined two experiments that demonstrate the capabilities of AFRL's adaptive receiver's capabilities. The fourth task, presented in this report, developed procedures for using the calibrated transponder in the radar cross section measurements of clutter and targets and demonstrated these procedures in the measurement of the local clutter environment.

Chapter 2.0 presents a brief review of the existing bistatic array receiver and its auxiliary equipment. Chapter 3.0 provides a brief review of the system's performance and the limitations associated with the equipment and the site environment. The capabilities and limitations of the calibrator for the measurement of radar cross section (RCS) and propagation are also reviewed.

Chapter 4.0 presents the calibration procedures for backscatter measurements. Subchapter 4.1 briefly discusses the preliminary procedures for setting up an experiment and performing the system equalization. The effects of the site environment and mainbeam multipath on the system calibration are described through the results of tests and experiments performed using the calibrated transponder. The use of a topographic map to help correlate the radar returns with physical features is also discussed. A method for translating the radar data from the polar coordinates of the bistatic receiver to the rectangular coordinate system of the maps is provided.

Subchapter 4.2 presents the calculation and use of a calibration constant for the radar cross section (RCS) measurement of point targets. The measurement procedures and system limitations are demonstrated through the measurement and presentation of the RCS of local structures and moving vehicles. Subchapter 4.3 extends the calibration procedures to the measurement of distributed clutter. Measurements of a local forest, a wooded hill and other areas using these procedures are presented. The last subchapter briefly discusses the use of the calibrator in measuring the attenuation through vegetation in support of experiments concerning the detection of screened moving vehicles.

This report concludes with a summary in Section 5.0.

2.0 REVIEW OF THE BISTATIC FACILITY

This section provides an overview of the bistatic system. The first section describes the bistatic receiver and its associated equipment used at the Newport test site from 1995 through September 1997. The second section summarizes the gain, distortion, channel-to-channel compensation and other performance measurements given in earlier reports. Provided are the system performance parameters such as gain-aperture product GA and system sensitivity δ that are used in the subsequent chapters. The section concludes with other measurements not previously reported.

Figure 2.1 shows the configuration of the Newport testbed during 1996. The system consists of several subsystems for waveform generation, control and data collection. The Intel-based Radisys VXI controller provides the user interface and control of the system and the DOS-based storage system for data. The Arbitrary Waveform Generator (AWG) provides a programmed waveform on a 5 MHz carrier to the up-converter. The output of the upconverter is manually transferred to either a calibration port for internal calibration or to the optical transmitter. The optical signal is received and demodulated at the transmitter site on Tanner Hill. This S-Band signal is provided to either the low power transmitter for array compensation measurements or to the high power transmitter for most experiments. The output of the bistatic receiver array is down-converted to a 5 MHz carrier, digitized and stored in an internal high speed buffer memory. The data is then transferred to the DOS-based storage in the controller. System coherence is maintained in the converter oscillators and the digitizers by locking all clocks to a 10 MHz reference.

A second optical system for remote control purposes was under development and was not used during 1996. Also shown is an auxiliary receiver using a 4 foot dish and a log amplifier. This subsystem is used during synchronization when the bistatic system is used with another host transmitter.

In 1997, the high power transmitter subsystem was moved to a location on Irish Hill. The 10 foot dish and pedestal were placed in a concrete pad on the northeast side of the main building with the transmitter placed in a nearby location within the building. The low power CW transmitter remained on Tanner Hill and used a sheltered 10 foot dish to provide a calibration signal. Use of the low power and high power transmitter required manually switching the optical output from the receiver at the optical junction box. Another change in 1997 is the use of a standard PC and MXI interface board in place of the Radisys controller.

Figure 2.1 Block diagram of bistatic receiver (August, 1996)

2.1 Waveform Generation and Up-Converter Subsystem

The waveform generation and up-converter subsystem provides calibration waveforms as well as radar transmitter signals for use at the Newport site. The waveform is generated using an HP 8770A Arbitrary Waveform Generator (AWG), a programmable device that provides waveforms with frequencies up to 50 MHz via a high-speed 125 MHz, 12 bit Digital-to-Analog Converter (D/A). Figure 2.2 shows the user console that houses the AWG in the lower shelf and the user console and test equipment in the higher shelves. The high dynamic range and high degree of oversampling allow the AWG to provide a high quality signal centered at 5 MHz. The manufacturer [9] sites phase linearity of +/- 5 degrees, harmonic distortion less that 50 dBc and single-sideband (SSB) phase noise of less than -120 dBc at a 10 kHz offset. Within the 2.5 MHz to 7.5 MHz passband of the receiver, the signal-to-phase-noise ratio (S/N) at the AWG output is approximately 60 dB. The AWG is programmed to provide different waveforms via a software interface developed by Rome Research, Inc. System coherence is maintained by phase-locking the AWG's internal sampling clock to the system's 10 MHz reference oscillator.

Figure 2.2 User console with computer display, AWG and test equipment

The AWG signals are up-converted to S-Band using the same LO sources as those used in the receiver. Figure 2.3 presents a block diagram of the up-converter fabricated by Rome Lab personnel. The noise contributed by the up-converter components include both thermal and phase noise components. The S/N limitation of the thermal noise components is approximately 80 dB, over 10 dB below the AWG noise level, and does not significantly impact the test signal's quality.

The primary phase noise contributors are the oscillator used to create the signal, the oscillator used to provide the A/D sampling clock and the two local oscillators used in frequency conversion. When the same oscillators are used in both the transmitter up-conversion and receiver

5

down-conversion, the phase noise power is a function of the short-term stability of these oscillators and the time delay t_d between transmission and reception. The power in the phase noise sidebands S(f) and the total phase noise N_{phase} can be given as [10,11]

$$S(f_m) = 4\left(\frac{\Delta f}{f_m}\right)^2 [\sin(\pi f_m t_d)]^2$$

$$N_{phase} = \int_0^{B_{coh}} S(f_m) df_m$$

where f_m is the offset frequency of the phase modulation, Δf is the frequency deviation in Hz and B_{coh} is the noise bandwidth of the receiver after coherent processing. For stable crystal oscillators, the fractional frequency deviation ($\Delta f/f_m$) is typically less that 10^{-5} at $f_m = 10$ kHz dropping to a floor of less than 10^{-7} at $f_m = 100$ kHz and higher offset frequencies. For the calibration measurements discussed in the next section, the time delay through the up-converter, calibration cables and the receiver is approximately 4 usec. For a noise bandwidth of 5.6 MHz, this results in a phase noise power of less than 60 dB below the carrier. With the stable VHF and microwave oscillators used in the system, the phase noise corresponding to such a small time delay is insignificant. However, at longer ranges or when another transmitter source is used, phase noise will become more important.

2.2 Optical and Transmitter Subsystem

The Newport test site consists of two hilltop sites that are approximately 6600 feet apart and 330 feet above the intervening valley. Optical fiber cable is available for the transmission of

Figure 2.3 Up-converter block diagram (October 1995) [6,8]

Figure 2.4 Optical transmitter [6,8]
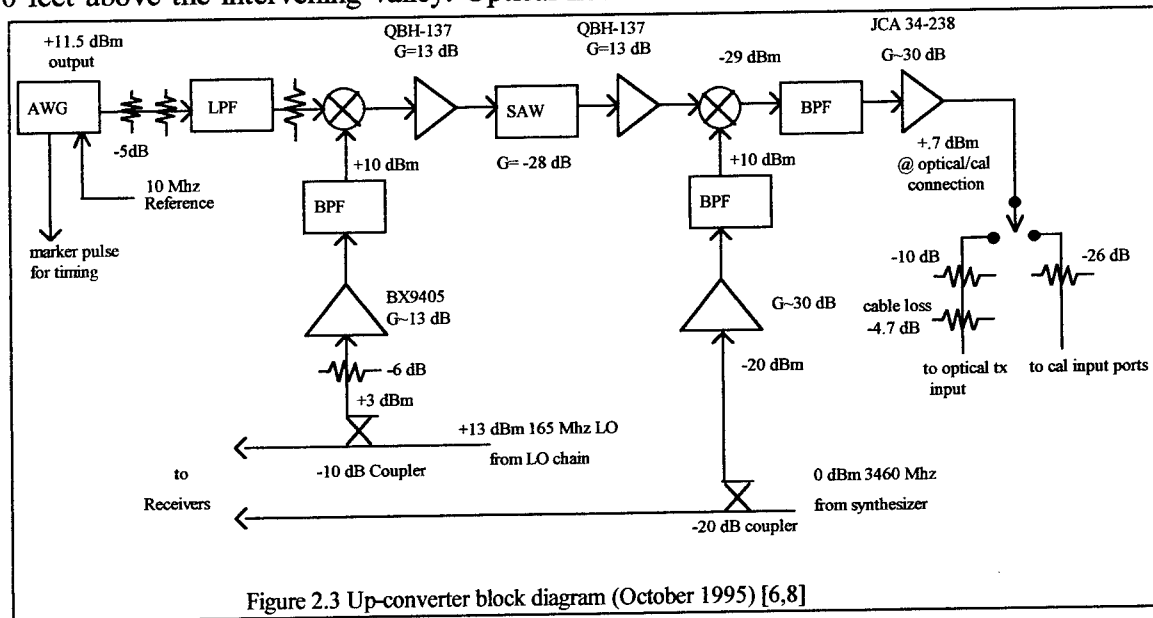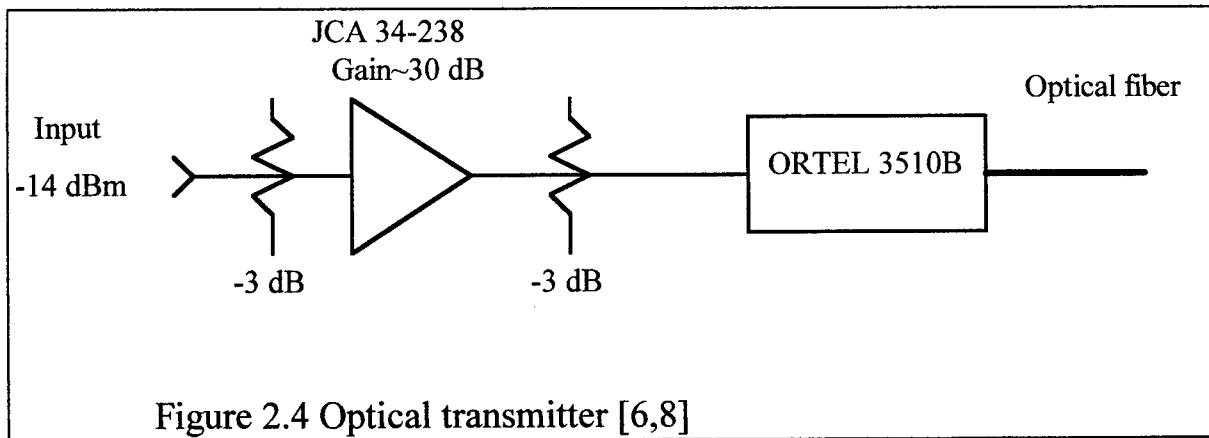
timing and RF signals between the Tanner Hill and Irish Hill sites. The bistatic testbed shelter is located on Irish Hill and uses this optical link to send transmit signals to a TWT transmitter located on Tanner Hill. The optical transceiver system consists of an Ortel 3510B optical transmitter and an Ortel 4508 optical receiver. As of 1997, a second optical transceiver system was to be installed to provide timing and remote control of the recently installed 1 kW (peak) pulsed transmitter and to allow remote monitoring of the parameters of the pulse transmitter, cw transmitter and the transmit antenna.

At S-Band, the maximum linear signal is obtained at the optical receiver with an input of +10 dBm into the optical transmitter. The loss in the optical system is approximately -52 dB and the measured signal-to-noise ratio (S/N) ratio at the output is approximately 45 dB. The measurement of optical loss is highly dependent on the quality and cleanliness of the optical cable connectors. Repeated removals and reinsertions of the fiber cable can easily provide several dB of change in the observed optical loss and S/N.

The third-order intercept point of the optical system is listed at over +25 dBm. This is not important for typical radar waveforms such as gated CW, pseudorandom phase codes and LFM, because such waveforms provide only one frequency at a given instant in time. Such waveforms can be transmitted at levels as high as +10 dBm input with good fidelity. However, tests using the simultaneous transmissions of multiple frequency waveforms require a compromise in total input power and fidelity.

Both low power (<25 watts) and high power pulsed TWT's have been discussed for use in future experiments. The low power transmitter is used primarily with a fixed antenna for receiver calibration and equalization. The 1 kW (peak) pulsed TWT uses a steerable 10 foot dish to provide signals for local experiments.
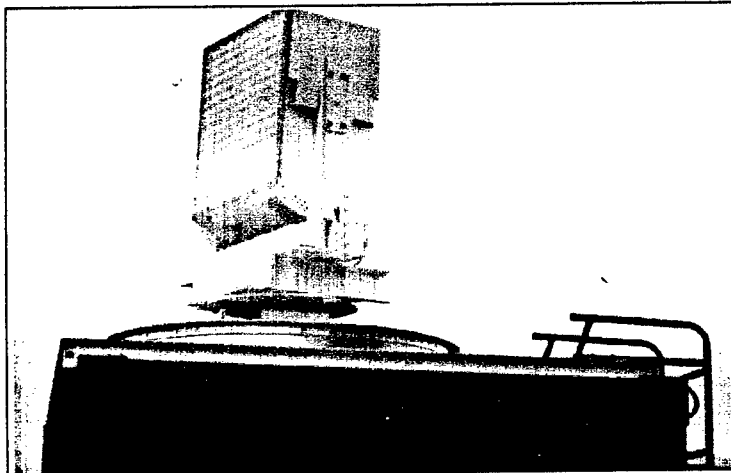
Figure 2.5 S-Band antenna (front view)

2.3 Antenna and Receiver Subsystem

Figures 2.5 and 2.6 show the front and rear view of the antenna respectively while Figure 2.7 shows the antenna with the radome in place. The antenna is a passive device consisting of 16 columns, each column consisting of 16 patch stripline antennas coupled with stripline couplers. The antenna is mounted on a pedestal that provides digital-controlled azimuth steering of plus or minus 180 degrees. The elevation angle is positioned manually from -8 degrees to + 8 degrees. In 1996, the front third of the radome plastic was replaced with clear Lexan to reduce loss.

Figure 2.8 shows a block diagram of the preamp assembly and the first mixer located in the receiver. The RF preamp modules are mounted near the column outputs to reduce the line lengths and the associated losses contributing to system noise figure. The hardline cables used between the antenna and the preamp assembly were carefully matched to preserve the gain and phase matching of the array outputs. Adjustable lines are also included to allow compensation of the phase differences in the preamp assemblies.

The preamp assembly's limiter is used to prevent damaging signal levels into the receiver while an SPDT switch provides further protection and reduces the

Figure 2.6 S-Band antenna (rear view)

8
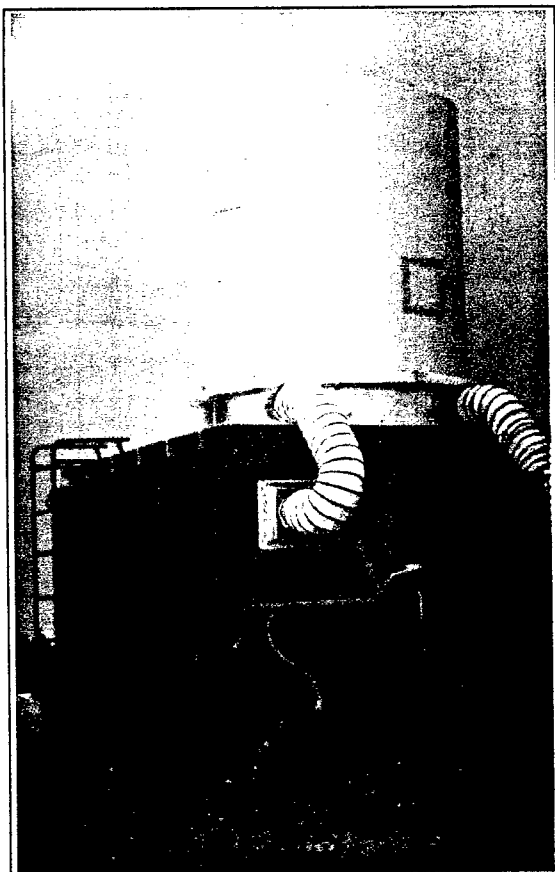
Figure 2.7 S-Band antenna with radome

interference from external signals during calibration tests. The -10 dB coupler allows the injection of a known signal for calibration and provides the test outputs used to form uniformly weighted sum and difference channels for setup and diagnostics.

When the system is in the calibration mode, the calibration signal is fed via hardline from the shelter to the antenna compartment where it is split into 16 channels, each channel associated with a column receiver. The measured loss and phase shift from the optical/cal switch to the coupler input are given in Table 2.1. The nominal loss is 18.2 dB at 3300 MHz with a (-.2/+.1 dB) variation from column to column. The variation over the 5 MHz band is within +/- .2 dB. The peak deviation of the phase from linear was less than 1 degree for each column.

Table 2.1 Measured amplitude loss in calibration cable

Column	3295 MHz Loss(dB)/phase(deg)	3300 MHz Loss(dB)/phase(deg)	3305 MHz Loss(dB)/phase(deg)
1	-18.1 / -32.1	-18.0 / -83.5	-17.9 / -134.5
2	-18.3 / -36.0	-18.3 / -86.7	-18.2 / -138.4
3	-18.3 / -48.1	-18.2 / -99.0	-18.2 / -151.2
4	-18.2 / -52.2	-18.2 / -102.8	-18.1 / -154.8
5	-18.1 / -22.8	-18.0 / -73.4	-17.9 / -125.6
6	-18.3 / -20.3	-18.1 / -71.5	-17.9 / -123.5
7	-18.3 / -46.8	-18.2 / -98.0	-18.1 / -149.8
8	-18.2 / -10.9	-18.2 / -61.8	-18.2 / -113.7
9	-18.3 / -28.1	-18.3 / -78.8	-18.2 / -130.8
10	-18.3 / -14.8	-18.3 / -65.7	-18.2 / -117.5
11	-18.4 / -30.3	-18.3 / -81.1	-18.2 / -132.8
12	-18.4 / -21.6	-18.3 / -72.5	-18.2 / -124.3
13	-18.4 / -32.3	-18.3 / -82.4	-18.2 / -133.7
14	-18.4 / -28.7	-18.3 / -79.7	-18.2 / -131.7
15	-18.4 / -25.8	-18.3 / -76.8	-18.2 / -128.5
16	-18.4 / -31.9	-18.3 / -82.5	-18.2 / -134.4

Figure 2.8 (labels):

Limiter 1
LL.~1 dB
1 dB comp.~+7 dBm
Po(max)~+20 dBm

SPDT
LL.~1dB
+20 dBm max
Isolation>60 dB

-10 dB RF
Coupler
LL.~.2 dB

Amp1
Gain=30 dB min.
NF=3 dB max
1 dB comp.~+10 dBm (nom)
BW: 2-4 Ghz

EQUIPMENT NOTES:
Limiter 1: M/A COM 2691-1015
SPDT: XB-55/XB-HA
-10 dB RF Coupler: KDI CA-671
Amp1: MITEQ AFD3-020040-30
BPF1: Salisbury Eng. CVB-4-3300-150

Antenna Column (16 active elements)

A

50 Ω

50

control

Calibration Signal Input

Test Output

BPF1
fc=3.3 Ghz
BW=150 Mhz
I.L.= 1 dB

Gain between A and B: 28 dB typ.

In Antenna Radome

Cable and connector loss

B

In Shelter

Added 8 dB attenuation

160 Mhz IF Output to IF Receiver

C

1st conversion module

Limiter

-10 dB

1st Conversion Module:
RHG DMT2-4/14EFC
NF~9.5 dB
Gain= 34 dB (TSC-H601-PD-008)
BW=50 Mhz (min)
Output @ 1 dB compression= +13 dBm
Channel-Channel Isolation = 40 dB

LO Input
+17 dBm nom.
3460 Mhz nom.
(3260-3660 Mhz)

splitter

test input: loss to RF-20 dB nom.

Figure 2.8 S-Band preamp and first mixer (December 1995) [8,12] (Modified 1996)

Figure 2.9 (labels):

Variable Attenuator
0 to 20 dB Range
Set to 10 dB

QBH-137
NF=4 dB
(Te=438°K)
Gain=13 dB

SAW BPF
Gain=-28 dB
BW=5 Mhz

QBH-137
NF=4 dB
(Te=438°K)
Gain=13 dB

D

E

SAW BPF

F

From 1st Mixer/preamp

G

QBH-137
NF=4 dB
(Te=438°K)
Gain=13 dB

MD-161
Gain ~ -6 dB

LO Input
0 dBm

To A/D Converter

QBH-195
G=17 dB
NF=3.5 dB

PLP-10.7
Gain @ 5 Mhz ~ -.5 dB
- 3 dB Gain @ 14 Mhz

QBH-172
G=15 dB
NF=3 dB

H

J

LPF

I

Figure 2.9 IF subsystem (December 1995) [6]

10

The preamps have a nominal noise figure of 3 dB and a minimum gain of 30 dB. The 4-pole bandpass filter has a bandwidth of 150 MHz to reduce the system's response to the image signals and the out-of-band interference. Matched lengths of hardline cable are used to transfer the 16 column signals from the bandpass filters located in the preamp assembly to the receivers located within the shelter.

An earlier interim document [6] characterized the receiver and made recommendations for improving the system's linear dynamic range. For a modest increase in noise figure (.85 dB), the linear

Figure 2.10 SAW IF filter response [Phonon Corporation]

dynamic range for third order distortion could be increased close to the limitation provided by the "10 "effective bits" advertized for the 11 bit A/D converter [13]. Since the system is used where the experimental parameters can be chosen to meet the S/N limitations and where the linear dynamic range is important, then the trade-off between linear dynamic range and noise figure is reasonable.

As shown in Figure 2.9, the receiver gain was reduced by 8 dB and the nominal linear dynamic range of the receivers was measured to be 66 dB [7]. The figure also presents a block diagram of the IF receiver. Most of the receiver's selectivity is provide by the surface acoustic wave (SAW) bandpass filter. Figure 2.10 presents the filter shape and general characteristics of these devices. The -3 dB bandwidth is nominally 5.6 MHz and a nominal rejection between -45 and -50 dB is obtained at offset frequencies from 4.8 MHz to 80 MHz. The Mini-Circuits PLP-10.7 low-pass filter provides additional selectivity, reducing adjacent channel signals and noise beyond 15 MHz .

The isolation between channels is limited by the LO chain (Figure 2.11). The RHG 3-channel mixer/preamps specify a 40 dB minimum isolation between the three channels contained within each module. The circulator and splitter provides an additional 40 dB of isolation between different modules. The 8-way splitter and the MD-161 mixers used in the second down conversion provide a minimum of 50 dB isolation.

11
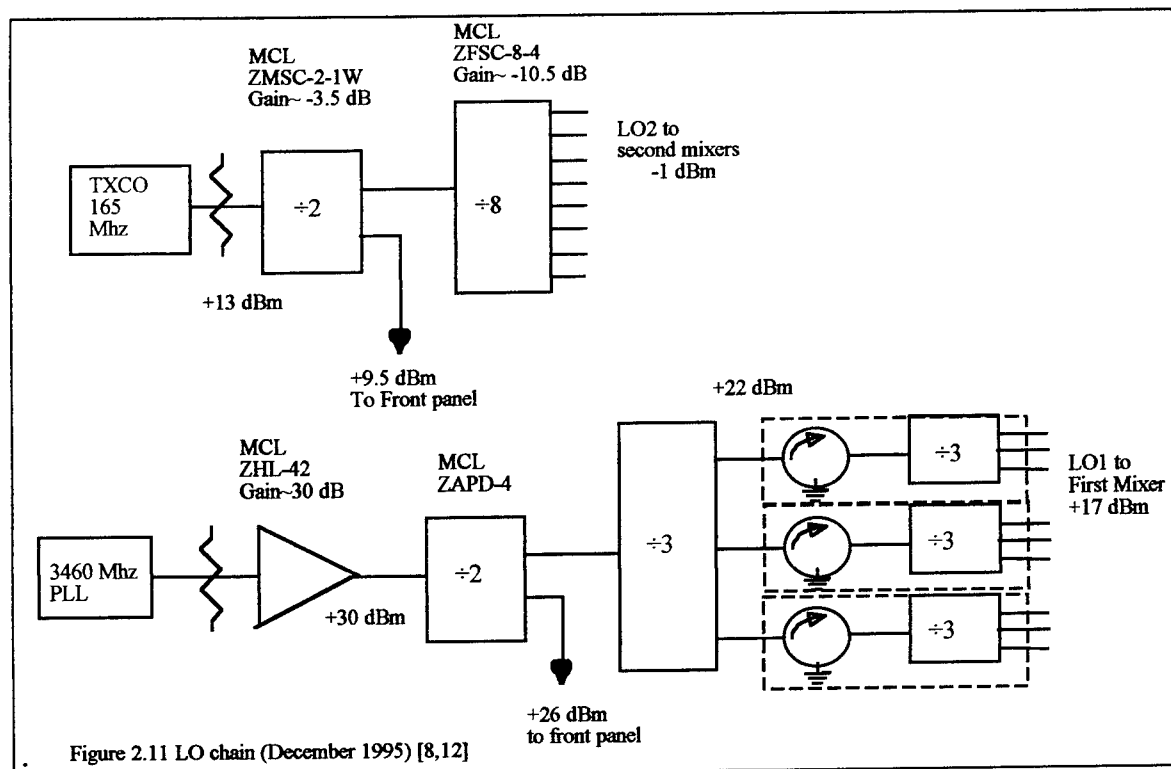
Figure 2.11 LO chain (December 1995) [8,12]

2.4 The A/D Converter, Digital and Timing subsystems

The original digital subsystem is a VXI-based system consisting of a Radisys 486-based controller, 8 dual-channel analog-to-digital (A/D) converters, VXI-based hard drives and an interface for logging GPS time. Each A/D converter is a HP E11429B digitizer, a dual-channel 12-bit VXI-based device capable of performing 20 million sample/second. Table 2.2 lists some of the specifications of these dual-channel converters. The harmonic distortion, at 61 dB down from a full scale signal, and the total noise and distortion of the A/D converters from all sources, at 59 dB down, are less than that created by the receiver's final amplifier. The timing of the bistatic receiver consists of several oscillators used for frequency conversion, A/D conversion and other timing. Coherence is maintained by locking the oscillators to a 10 MHz reference.

The manufacturer claims that the 1 volt, 50 ohm single-ended range provides the most linear A/D performance. The Least Significant Bit (LSB) signal specifies a sinusoidal signal at the A/D converter with an rms value equal to the LSB. For an 12 bit A/D converter operated in its +/- 1 volt bipolar mode (11 bits plus sign), the digital output has a range from +2046 for a 1.023 volt peak input to -2045 for a -1.0225 volt peak input. (-2048, -2047, -2046 and 2047 either indicate overload or are not used.) The LSB corresponds to 1.023/2047 = .0005 volts. An LSB signal within an rms value of .0005 volts into 50 ohms would have an average power of -53 dBm.

12

Each digitizer contains a 512 Kword (1 MByte) buffer memory that can be partitioned for multiple recordings using software. The recorded data can then be transferred to the Radisys DOS-based drive or to a VXI drive or processor.

In 1997, a standard PC and a MXI interface board replaced the Radisys controller to provide more flexibility, more data storage and a better user interface. A software interface to a VXI drive was also developed for faster HP Local Bus transfers. The advertised transfer rate of the buffer memory data to other devices was 2-4 MWord/second via the VME bus and 20-40 MWord/second via the HP Local bus. However, the observed transfer rates were significantly less. During September 1997, the observed HP local bus transfer rate from the digitizers to the VXI disk drive was on the order of 20 MBytes/second while the transfer of the data from the VXI drive to the DOS drive was on the order of 64 KBytes/sec. Development is continuing on this software to improve speed and reliability. The transfer rate from the digitizers to the DOS drive using the Rome Research software was in the order of 10 KBytes/second. While this transfer is slow, it is very reliable and was used to record the data presented in this report.

Table 2.2 Specifications of the HP E1429A/B 20 MSa/s 2-Channel Digitizer [13]

Resolution:	12 Bits (11 Bits + sign)
	-2045 to +2046 on-scale readings
Sample rate:	20 Million samples/sec
Effective number of bits:	10.3 bits typical for 500 kHz signal
(4.5.2; 4.1.3)***	9.8 bits typical at 10 MHz signal
Harmonic distortion:	-64 dB THD at 500 kHz (THD includes 2nd through 6th harmonic)
(4.4.2.1)***	-61 dB THD at 10 MHz
Signal-to-Noise Ratio:**	62 dB at 500 kHz
(4.5.1)***	59 dB at 10 MHz
Differential Nonlinearity:	1 LSB
(4.4.1.2)***	
Integral Nonlinearity:	2 LSB
(4.4.3)***	
Memory:	512K readings (1 MByte)
	Partitionable in to 2^n segments where n = 0 to 7
Input Voltage Range:	-0.10225 to 0.10230 V / 50 ohm
	-0.2045 to 0.20460 V / 50 ohm
	-0.51125 to 0.51150 V / 50 ohm
	-1.0225 to 1.02300 V / 50 ohm
Analog Bandwidth:	> 50 MHz (1 V range)
(4.6.1)***	> 40 MHz (other ranges)
Cross-talk:	-80 dB, DC to 10 MHz
(4.11)***	
Read-Out Speed:	
VME Bus	up to 2 M readings/sec (16 bit transfers)
	up to 4 M readings/sec (32 bit transfers)
Local Bus*	up to 20 M readings/sec (either channel separately)
	up to 40 M readings/sec (both channels interleaved)

* readings may be routed to Local Bus during digitization and simultaneously with recording in the internal memory
** includes noise, distortion and all other undesired effects as defined in IEEE 1057
*** refers to sections in IEEE Standard 1057

3.0 SYSTEM PERFORMANCE AND CALIBRATION

An interim report [7] discussed the issues in calibrating the bistatic system. These issues included compensation for the phase and amplitude distortion for each channel, equalization of the channel-to-channel variations and calibration of the multi-channel receiver for the measurement of bistatic radar cross of clutter targets. A later report [35] presented the measured results of the implemented compensation, equalization and calibration routines and provided measures of system performance. This section summarizes those results and provides the formulas and values that are used in the presentation and discussion of the bistatic calibration results presented in later sections. The radar range equations given in (3.1) and (3.2) provide the typical parameters of interest in a radar application.

$$(3.1) \quad S = \left(\frac{P_t G_t(\theta_t, \phi_t)}{L_t} \right) \left(\frac{F_t^2}{4\pi R_t^2 L_{et}} \right) \left(\frac{\sigma_t}{1} \right) \left(\frac{F_r^2}{4\pi R_r^2 L_{er}} \right) \left[\left(\frac{\bar{A}_{col}}{\bar{L}_{col} \bar{L}_r} \right) \left(\frac{N_{col}}{L_{wta}} \right) \left(\frac{\bar{G}_r}{1} \right) \left(\frac{\mathcal{R} N_p}{L_{wtr} L_{wtp}} \right) \right]$$

$$(3.2) \quad \frac{S}{N} = \left(\frac{P_t G_t(\theta_t, \phi_t)}{L_t} \right) \left(\frac{F_t^2}{4\pi R_t^2 L_{et}} \right) \left(\frac{\sigma_t}{1} \right) \left(\frac{F_r^2}{4\pi R_r^2 L_{er}} \right) \left[\left(\frac{\bar{A}_{col}}{\bar{L}_{col} \bar{L}_r} \right) \left(\frac{N_{col}}{L_{wta}} \right) \left(\frac{\mathcal{R} N_p}{L_{comp} L_{wtr} L_{wtp}} \right) \left(\frac{1}{\kappa \bar{T}_s B_n L_{AD} L_{IQ}} \right) \right]$$

The terms are defined in Appendix A. Two useful parameters are defined in this report to allow a quick assessment of the bistatic receiver performance with a host transmitter. These parameters are the receiver's gain-aperture product and the receiver's sensitivity.

3.1 Gain-Aperture Product

One parameter is the gain-aperture product GA

$$GA = \left[\left(\frac{\bar{A}_{col}}{L_{radome} \bar{L}_{col} \bar{L}_r} \right) \left(\frac{N_{col}}{L_{wta}} \right) \left(\frac{G_r}{L_{comp_s}} \right) \left(\frac{\mathcal{R} N_p}{L_{wtr} L_{wtd}} \right) \right]$$

which relates the power density at the face of the array to the output power of the processed signal. The parameters grouped in parentheses are the column aperture and passive RF losses, beamforming gains and loss, receiver gains including compensation loss and signal processing gains and losses.

The measurements of the column aperture and passive RF losses

$$\left(\frac{\bar{A}_{col}}{L_{radome} \bar{L}_{col} \bar{L}_r} \right)$$

were discussed in an earlier report [7]. The column weighting was uniform and the average directive aperture $\bar{A}_{col}$ was calculated as .046 m^2 based on physical measurements of the array. The product of the radome loss L_{radome}, the average passive RF loss within the column $\bar{L}_{col}$ and the average passive RF losses preceding the RF preamplifier and signal injection circuitry was measured as 8.13 or 9.1 dB.

The number of columns in the testbed array N_{col} is 16. The loss in the beamforming network L_{wta} is a function of the weighting used and ranges from 1 for uniform azimuth weighting to over 2 for low sidelobe weightings. L_{wta} is treated as a signal processing loss.

The receiver gain G_r includes the gains and losses from the input to the RF preamplifier to the input of the digital compensation and equalization filter. The average analog gain $\bar{G}_r$ of the receiver from the input of the RF preamplifier to the input of the A/D converter is 54.3 dB. The signal gain of the A/D converter is set to unity. The digital demodulator (digital IF-to-quadrature detector) incorporates a digital amplification of 2 to provide unity gain. The compensation filter normalizes each channel gain to the gain of the first channel and equalizes the amplitude and phase difference across the 5 MHz passband. This average signal loss L_{comp} is 1.2 or .8 dB.

The weighting used in the azimuth beamforming are normalized such that the maximum signal power gain from an N column array is N_{col} with uniform weighting. Similarly, the weighting used in Doppler filtering and matched filtering are also normalized to provide maximum signal gains of N_p and $\mathcal{R}$, respectively. When nonuniform weighting is used, there is a loss in signal gain relative that can be calculated in the form

$$L_{wt} = \frac{Loss_{noise}}{Loss_{sig}} = \frac{\left| \sum_{n=1}^{n=N} \left(wt(n)\right)^2 \right| N}{\left| \sum_{n=1}^{n=N} wt(n) \right|^2}$$

where the weights wt are calculated to provide unity noise gain.

$$Loss_{noise} = \left| \sum_{n=1}^{n=N} \left(wt(n)\right)^2 \right| = 1.$$

Thus, for an N column array,

$$L_{wta} = \frac{Loss_{noise}}{Loss_{sig}} = \frac{N_{col}}{\left| \sum_{n=1}^{n=N_p} wta(n) \right|^2}$$

and the net gain of the beamforming network is

$$G_{beamform} = \frac{N_{col}}{L_{wta}} = \left| \sum_{n=1}^{n=N_{col}} wtd\,(n) \right|^2 .$$

Similar relationships exist for the net gain of Doppler filtering and matched filtering.

Therefore, the gain-aperture product can be written as

$$GA = \left[\left(\frac{.046}{8.13} \right) \left(\frac{16}{L_{wta}} \right) \left(\frac{269*10^3}{1.2} \right) \left(\frac{\ell N_p}{L_{wtr} L_{wtd}} \right) \right]$$

$$GA = 20.3*10^3 \left(\frac{\ell N_p}{L_{wta} L_{wtr} L_{wtd}} \right)$$

$$GA_{dB} = 43.1 + 10\log \left(\frac{\ell N_p}{L_{wta} L_{wtr} L_{wtd}} \right)$$

When used with a transmitter in a bistatic geometry, the output signal power can be related to target RCS and range by

$$S = \left(\frac{P_t G_t}{L_t} \right) \left(\frac{F_t^2}{4\pi R_t^2 L_{et}} \right) \left(\frac{\sigma_t}{1} \right) \left(\frac{F_r^2}{4\pi R_r^2 L_{er}} \right) GA$$

The local measurements at the Newport site used a 1 kW transmitter and a 10 foot dish. The transmitter power was measured at the feed and includes the transmitter line loss. The typical transmitter power at the feed was 300 watts. The ideal directive gain of a 10 foot dish at S-band is 10965 or 40.4 dB. The remaining transmitter loss L_t is the feed illumination loss. This loss was not measured and a typical value of 1.5 dB was used in the theoretical estimates. The typical measurement waveform was 40 microsecond linear frequency waveform with a 5 MHz bandwidth and ℓ equals to 200. The number of pulses N_p ranged from 16 to 128. For $N_p = 16$ and uniform weighting in the azimuth beamforming, Doppler filtering and matched filtering,

$$S_{dBm} = 54.8 + 40.4 - 1.5 - 11 - 11 + 10\log \left(\left(\frac{F_t^2}{R_t^2 L_{et}} \right) \left(\frac{\sigma_t}{1} \right) \left(\frac{F_r^2}{R_r^2 L_{er}} \right) \right) + 43.1 + 23 + 12$$

$$S_{dBm} = 149.8 + 10\log \left(\left(\frac{F_t^2}{4\pi R_t^2 L_{et}} \right) \left(\frac{\sigma_t}{1} \right) \left(\frac{F_r^2}{4\pi R_r^2 L_{er}} \right) \right)$$

17

3.2 Sensitivity

A second useful parameter, the system sensitivity $\mathcal{L}$

$$\mathcal{L} = \left[\left(\frac{GA}{\bar{G}_r \, L_{collapse} \kappa \bar{T}_s \, B_n L_{AD} L_{IQ}} \right) \right]$$

relates the power density at the face of the array with the signal-to-noise ratio at the system output.

The noise power at the output is a function of the receiver noise $\kappa \bar{T}_s \, B_n$ and the additional noise contributed by other processing. κ is Boltzmann's constant with a value of $1.38*10^{-20}$ milliwatt-seconds (-198.6 dBm-sec). The noise bandwidth B_n is equal to the smaller of the analog receiver's bandwidth (5.6 MHz) and the -3 dB bandwidth of the transmitted waveforms matched filter. The average system noise temperature of the bistatic testbed receivers is 663 °K as discussed in an earlier report. [7]

The average receiver gain $\bar{G}_r$ for noise is the same as that for the signal, 54.3 dB. The analog-to-digital converter injects noise through aliasing, quantization and time jitter.[35]. The aliasing noise is a function of the input noise bandwidth and the sample rate. The receiver noise is dominated by the noise within the 5.6 MHz bandpass. The noise generated by the post IF filter amplifiers are further attenuated by the internal A/D filters. The resultant aliasing noise is less than .1 dB and is ignored. The quantization loss is a function of the input noise to LSB ratio. For the normal operation where the average receiver noise into the A/D converter is -48.6 dBm. This corresponds to an rms voltage of .83 mv or 1.7 quantums. For weak signal conditions where the additive A/D noise is dominated by the quantization noise,

$$L_{A/D} = 10\log(1+\frac{\sigma_A^2}{\sigma_n^2}) = 10\log(1+\frac{(.14)^2}{(.83)^2}) = .1dB \,[1].$$

The noise generated by time jitter or aperture uncertainty is a function of the input signal level. For small signal levels, this noise is well below the thermal noise. For signals approaching saturation, the time jitter noise can approach .9 mv. Operation at levels approaching saturation is normally avoided to prevent additional losses due to saturation. Typical operation is to provide at

---

[1] This corrects an error in [35, page3-7]

18

least a 3 dB margin to prevent saturation. For these signal levels, a reasonable estimate of noise from time jitter is .63 mv. Therefore, $L_{A/D}$ can be given as

$$L_{A/D} = 10\log\left(\frac{\sigma_n^2 + \sigma_\Delta^2 + \sigma_{ap}^2}{\sigma_n^2}\right) = 10\log(1 + \frac{\sigma_\Delta^2 + \sigma_{ap}^2}{\sigma_n^2}) = 10\log(1 + \frac{(.14)^2 + (.63)^2}{(.83)^2}) = 2.1 dB.[2]$$

The digital IF-to-quadrature process used the Hilbert transform process given in several references [7,26-29]. Fourier transforms of twice the sample window are used to eliminate the increase in noise due to foldover. The signal gain of the digital IF-to-quadrature process was set to unity. However, the S/N loss L_{IQ} is about 2 or 3 dB [7].

The channel equalization and compensation filters compensate for each filter non-ideal amplitude and phase characteristics within the passband and adjusts the gain within each channel to provide 53.5 dB of net signal gain. However, the equalization does not equalize the noise in each channel. When the channels are added vectorially in the beamforming process, the addition of non-equal noise levels provides a collapsing loss $L_{collapse}$ of 1.02 or .1 dB.

Therefore, the system sensitivity can be given as

$$\delta = \left[\left(\frac{GA}{(269*10^3)(1.02)(1.38*10^{-20})(633)B_n(1.6)(2)}\right)\right]$$

$$\delta = \left[\left(2.65*10^{15}\left(\frac{\Re N_p}{B_n L_{wta} L_{wtr} L_{wtd}}\right)\right)\right]$$

$$\delta = \left[\left(154.2 + 10\log\left(\frac{\Re N_p}{B_n L_{wta} L_{wtr} L_{wtd}}\right)\right)\right].$$

For most of the local measurements performed at the Newport site, B_n = 5 MHz and

$$\delta = \left[\left(87.2 + 10\log\left(\frac{\Re N_p}{L_{wta} L_{wtr} L_{wtd}}\right)\right)\right].$$

When used with a transmitter, the signal-to-noise ratio at the receiver output can be related to the target size and range by

---

[2] This corrects an equation given in [35, page 3-7]

19

$$\frac{S}{N} = \left(\frac{P_t G_t}{L_t}\right)\left(\frac{F_t^2}{4\pi R_t^2 L_{et}}\right)\left(\frac{\sigma_t}{1}\right)\left(\frac{F_r^2}{4\pi R_r^2 L_{er}}\right).$$

Substituting the local measurement parameters given earlier,

$$\frac{S}{N}_{dB} = 54.8 + 40.4 - 1.5 - 11 - 11 + 10\log\left(\left(\frac{F_t^2}{R_t^2 L_{et}}\right)\left(\frac{\sigma_t}{1}\right)\left(\frac{F_r^2}{R_r^2 L_{er}}\right)\right) + 87.2 + 23 + 12,$$

$$\frac{S}{N}_{dB} = 193.9 + 10\log\left(\left(\frac{F_t^2}{R_t^2 L_{et}}\right)\left(\frac{\sigma_t}{1}\right)\left(\frac{F_r^2}{R_r^2 L_{er}}\right)\right).$$

Ignoring the propagation factors and small atmospheric losses, a signal-to-noise ratio equal to or exceeding 20 dB can be obtained for a one square meter target at bistatic ranges R_b up to 12 nm. For the Newport measurements, at normal experiment ranges of about 2 nm, this S/N can be maintained for up to 30 dB of two-way propagation attenuation for a one square meter target and up to 50 dB of two-way propagation attenuation with a 20 dBsm calibrator signal.

Table 3.1 Summary of System Parameters [35]

$\bar{A}_{col} = .046 \text{ m}^2$ (-13.4 dBsm)

$L_{radome} \, \bar{L}_{col} \, \bar{L}_r = 8.13 \, (9.1 dB)$

$N_{col} = 16$

$$L_{wta} = \begin{cases} 1 \text{ (for uniform weighting)} \\ 1.3 \text{ (for Taylor weighting } \bar{n} = 6, \text{ SL} \\ > 1 \text{ for other nonuniform weightings} \end{cases}$$

$G_r = 53.5 dB$

$L_{comp_s} = 1.023 \, (.1 db)$

$\mathcal{R} = 200$

$N_p = 16$

$$L_{wtr} = \begin{cases} 1 \quad \text{for uniform weighting} \\ 1.4 \text{ for Hamming weighting} \end{cases}$$

$$L_{wtd} = \begin{cases} 1 \quad \text{for uniform weighting} \\ 1.4 \text{ for Hamming weighting} \end{cases}$$

$\kappa = 1.38 \times 10^{-23} \text{ watt - second} / ^\circ K$

$\bar{T}_s = 663 ^\circ K$

$B_n = 5 MHz$

$L_{IQ} = 2$

3.3 Calibration

The existing S-Band multichannel receiver is to be used in performing bistatic experiments and concept evaluations in support of the Advanced Offboard Bistatic Technology effort. These bistatic experiments include the measurement of the bistatic RCS and spectra of natural and manmade structures, aircraft and vehicles, the measurement of the bistatic RCS and spectra of terrain clutter, sea clutter and weather clutter and the testing of multi-domain adaptive processes against jamming and clutter. These measurements are made in support of the development and evaluation of several bistatic adjunct receiver concepts in both strategic applications such as gap filling between monostatic sensors and in covert tactical applications.

These tests can provide useful and repeatable information only if proper calibration is performed during the measurements. The term calibration is used in its most general sense. That is, calibration is a method for quantifying the observations and conditions of an experiment such that the experiment, when reproduced by others, will provide repeatable results. This not only requires that the equipment be calibrated such that the imperfections of the bistatic recording system are compensated for and powers, voltages, losses and gains are measured accurately. It also requires that the ground-truth associated with the measurement be recorded and the definitions used in creating the results be clearly and concisely presented.

For example, consider a measurement of the mean and distribution of homogeneous land clutter. The term "homogeneous" means that each cell within a region has some set of similar properties. While the concept is clear, the implementation is not standardized. Some might map the terrain into homogeneous areas based on physical features (local slope, vegetation, etc.) while others might create a map based on radar reflectivity statistics (mean, spread, correlation length). It is not obvious that the two maps would be the same. Thus, results using the first criterion may be of limited use to those interested in homogeneity based on the second criterion. Furthermore, if results were given without reference to the criterion used, the results are best considered antidotal. Therefore, to get calibrated and repeatable results, the ground truth and criterion used in the analysis must be part of the calibration process.

The type and nature of ground-truth data needed to quantify measurements are often interdisciplinary and are highly dependent on the factors that the analyst believes impacts the measurement results. This is especially true for clutter measurements where the RCS, Doppler and other echo characteristics are highly dependent on a variable natural environment. Therefore, the bistatic testbed can only provide the ability to record and tag a number of auxiliary data files that each experiment can redefine as needed.

For short range measurements of point targets in free space, knowledge of the system losses and other radar parameter can allow the use of the radar range equation to estimate the RCS of the target. During the summer of 1997, measurements were made of the bistatic radar system using a calibrated transponder designed and fabricated at Rome Lab. Details of this calibrator and the results of the experiments are given is another report [35]. These measurements show a difference of less than one dB between the estimate using the system parameters and the radar range equation and the estimate using a calibrated transponder.

3.3.1 Calibrated Transponder

The calibrated transponder simulates a target of known radar cross section (RCS). If the transmitted energy intercepted by a target can be represented by its aperture in the direction of the transmitter $A(\varphi_t)$ and the gain of the reradiation pattern in the direction of the receiver can be represented by $G(\varphi_r)$, then the RCS of a target can defined as

$$RCS_{t\arg et}(\varphi_t, \varphi_r) = A(\varphi_t)G(\varphi_r)$$

Calibrated transponders operate in a similar fashion where a range of RCS values can be simulated using gain G_a. With the receive aperture pointed in the direction of the transmitter and transmit aperture pointed at the bistatic receiver,

$$RCS_{transponder} = A_e G_a G$$

The transponder can be used without modulation in a benign clutter environment. However, for field use with the bistatic system, the clutter from the terrain and vegetation within the same resolution cell as the calibrator can easily equal or exceed the RCS of the calibrator. To use the transponder effectively, the signal can be phase modulated to distinguish the calibration signal from the surrounding clutter. Sophisticated tools are commercially available to provide both amplitude and Doppler modulation simulating target motion [21]. A simple well-known phase modulator is a serrasoid modulator [38]. This modulator consists of a 360 degree digital phase shifter and a sawtooth digital driver. For an input S-band sinusoidal signal $A \cos(\omega t)$, the output of an ideal modulator is

$$S_{out} = kA \cos[\omega t + \phi(\omega_d)]$$

where $\phi(\omega_d) = 2\pi x(t)$, x(t) is a periodic sawtooth waveform of period T_d

$$x(t) = \begin{cases} \dfrac{t}{T_d - t_{recover}} & \text{for} \quad 0 < t < T_d - t_{recover} \\ 1 - \dfrac{t - (T_d - t_{recover})}{t_{recover}} & \text{for} \quad T_d - t_{recover} < t < T_d \end{cases}$$

and $f_d = 1/T_d$ is the desired modulation frequency. The parameter k presents the product of the phase shifter's passive loss and modulation efficiency. Figure 3.1 shows the spectrum using an ideal modulator. The modulation frequency contributes a single sideband modulation component while the other components represent the frequency components of a sawtooth waveform.

Figure 3.2 presents an implementation of the calibrator used in 1997. The receive and transmit aperture was provided using standard gain S-band horns with a gain of 16.5 dB at 3.2 GHz. The effective aperture of each horn can be given as

$$A_e = A_{physical}\eta_e = \frac{\lambda^2 G}{4\pi} = \frac{(.094)^2(44.7)}{12.566} = .031 \ m^2 \ (-15.1 \ dBsm).$$

The gain G of each horn at the operating frequency of 3.3 GHz. is 16.4 dB.
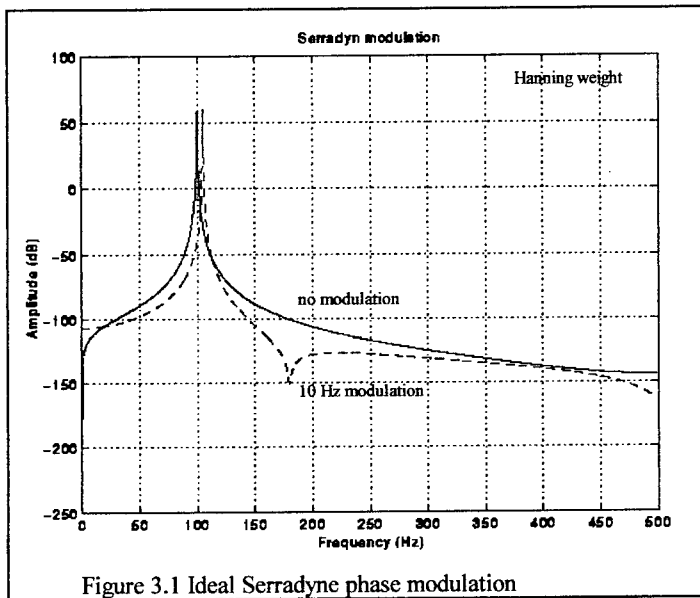
Figure 3.1 Ideal Serradyne phase modulation

The total gain of the modulator is $G_a = \frac{kG_1}{L_1 L_2}$ where G_1 is the gain of the amplifier, L_1 is the loss of the input cable and L_2 is the loss of the output cable.

The calibrator used an 8-bit S-band phase shifter, an 8-bit A/D converter and a function generator to provide the sawtooth waveform. This implementation was used because it could be quickly assembled. However, it had several non-ideal aspects. First, the sawtooth waveform was not ideal,

Figure 3.2 Block diagram of calibrated transponder used in 1997

Figure 3.3 Closed loop measurement of transponder with no modulation and prf of 1000 Hz.

Figure 3.4 Closed loop measurement of transponder output with a modulation frequency of 200 Hz and a prf of 1000 Hz.

Figure 3.5 Closed-loop measurement of the transponder with a modulation frequency of 500 Hz and a prf of 1000 Hz.

providing the desired ramp over only 95% of the period. Second, the phase shifter provided a small amplitude variation as a function of phase. Figures 3.3 through 3.5 present closed loop measurements of the transponder output without and with modulation. The input signal was a pulse with a pulse width of 40 usec and a prf of 1000 Hz. Figure 3.3 shows the output with no intentional modulation. A small amount of modulation due to clock leakage is evident below -20 dBm, about 55 dB below the 35 dBm signal.
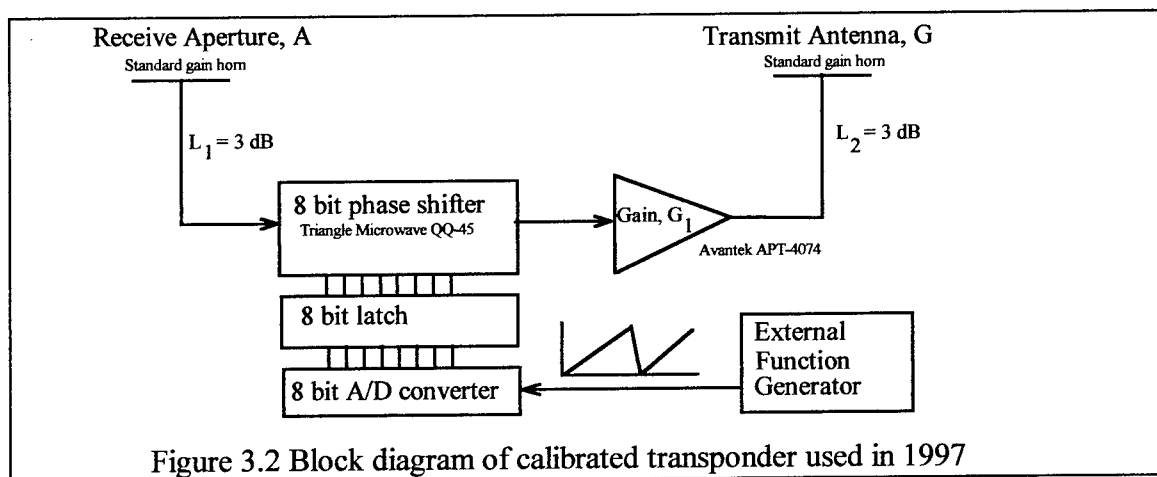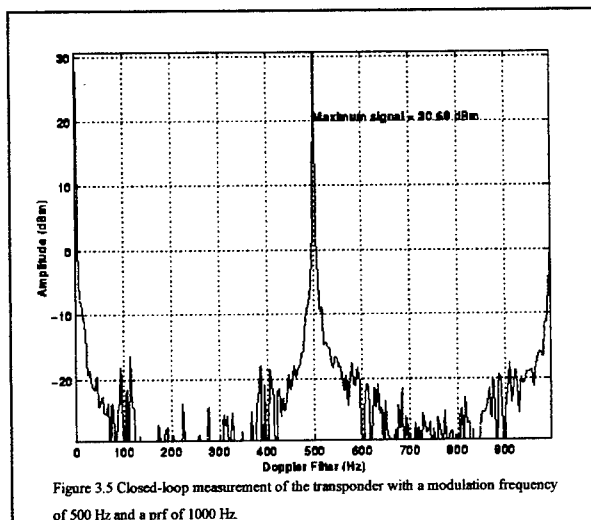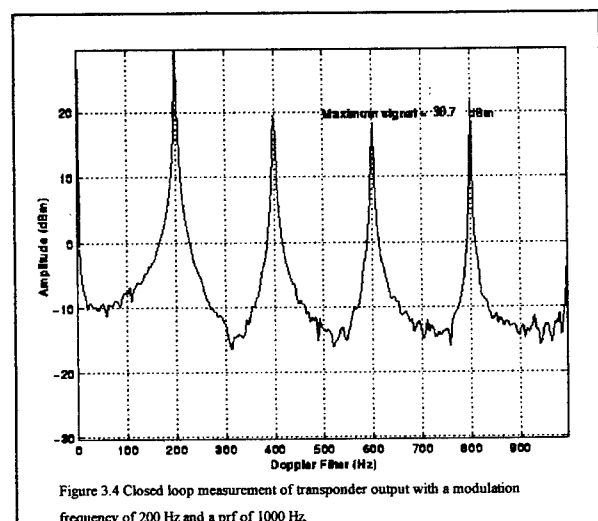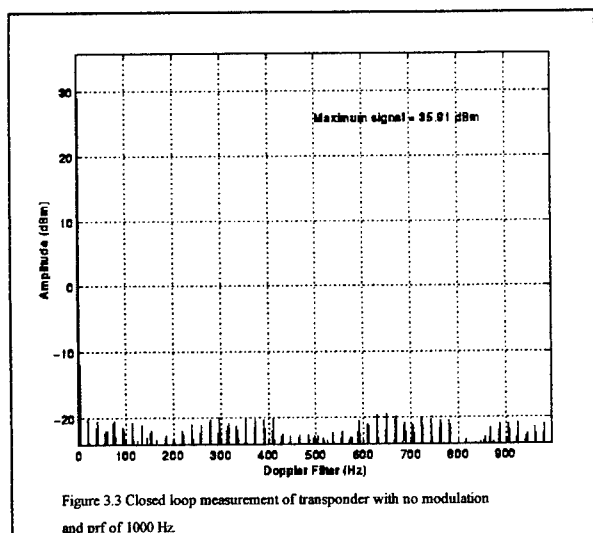
Figure 3.4 shows the calibrator output with a 200 Hz modulation. The harmonics of the 200 Hz modulation frequency is created by the non-ideal sawtooth signal, the variable attenuation of the phase shifter and the 8-bit phase quantization. The modulated signal level of 30.7 dBm represents a loss of 5.2 dB from the unmodulated signal level. Figure 3.5 shows the modulated output using a 500 Hz modulation frequency or half the prf.

The measured gain of the modulator and amplifier (kG_1) for the unmodulated signal was 30.0 dB and G_a = 30.0-3-3=24 dB. The effective RCS of the calibrator with no modulation is

$$RCS_{dB} = -15.1 + 24 + 16.4 = 25.3 \; dBsm.$$

For the modulated signal, kG_1 = 24.8 dB and G_a = 24.8-3-3=18.8 dB. The effective RCS of the calibrator with modulation is

$$RCS_{dB} = -15.1 + 18.8 + 16.4 = 20.1 dBsm.$$

In 1998, an improved and more mobile version was fabricated for Rome Lab by Mr. Kevin Besig of Rome Research Corp. The external function generator was replaced by an internal

25

microprocessor-controlled ramp generator that provided a near ideal ramp. The microprocessor was programmed such that the phase modulation frequency was entered by the user directly using rotary switches. The separate tripods for the standard gain horns were also replaced with a single tripod scheme where the receive and transmit horns were placed on a single four foot horizontal beam. The net amplification of the system was also increased resulting in an effective RCS of 33.1 dBsm.

3.3.2 Field Tests

One use of the calibrator is to provide a known RCS reference for the measurement of targets and clutter. If the calibrator were used in free space, the only sources of error would be the pointing error of the antenna, the signal-to-noise-plus-interference ratio and the difference in the propagation loss at the calibrator and the target or clutter of interest. However, since the calibrator is used near the earth, another source of error is multipath. Therefore, it was important to find a site and a procedure where the errors from multipath were minimized.

Several easily accessible sites were investigated within two miles of the Newport site. A good site providing repeatable data with little multipath was found near the town barn in Newport, NY. Figures 3.6a and 3.6b show the view from the calibration site toward the transmitter and receiver, respectively. The site had an unobstructed view of both the transmitter and the receiver on Irish Hill. The terrain in the area where a specular multipath would be

Figure 3.6a View toward transmitter [40]   Figure 3.6b View to receiver [40]

expected was rough with tall grass with a wire fence and hedge of small bushes providing a natural multipath fence. Figure 3.7 shows the measured multipath at this site. The ideal multipath cases in dashed lines are normalized to 0 dBm while the solid line represents measured values. The lack of strong lobing indicates that the multipath scatter is significantly reduced, providing a near uniform amplitude versus height.

One-way and bistatic measurements were taken on several days. Mr. Kevin Besig of Rome Research Corporation operated the transmitter while Ms. Elaine Kordyban performed the one-way field measurements and aligned the calibrator for the two-way measurements. The one-way measurements used a 40 microsecond unmodulated pulse at a PRF of 2 msec. An HP 8559A spectrum analyzer was calibrated to relate the peak displayed power density to peak power. With peak input power of -21.2 dBm, this waveform displays a peak power density of -29 dB using the measurement settings. Table 3.2 shows the measured power intercepted by one of the calibrator's standard gain horns and represents the input power to the calibrator P_{cal}. For comparison, the one-way power estimated from

$$P_{cal} = \frac{P_t G_t A_e F_t^2}{4\pi R_t^2 L_a L_c L_t}$$

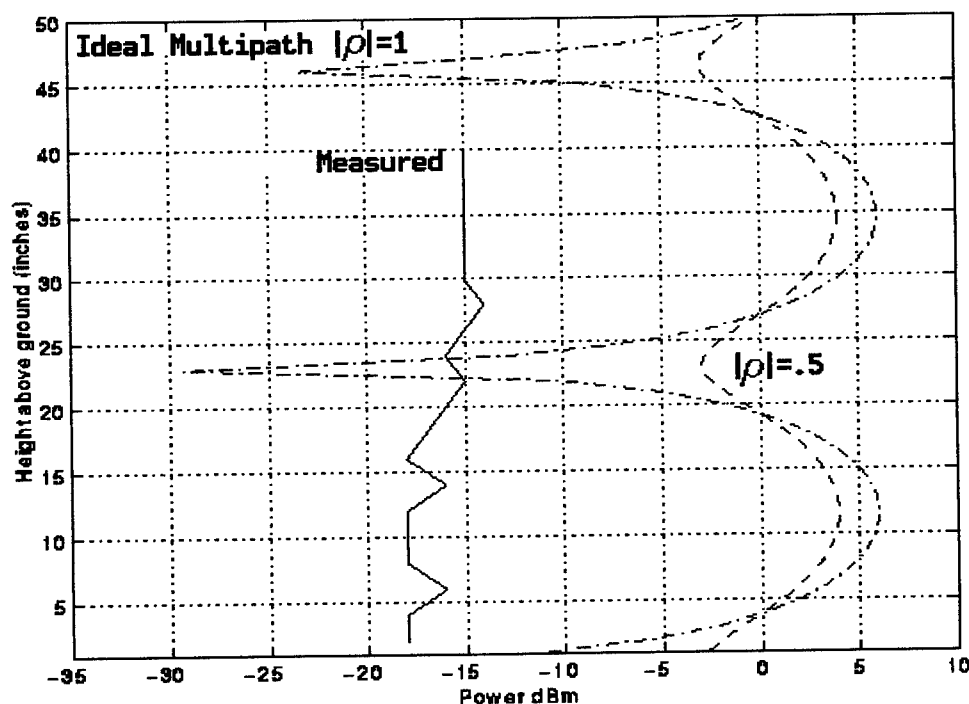is also provided. Constants in this equation are the transmit antenna gain G_t=10,965 (40.4 dB),

Figure 3.7 Theoretical and measured multipath at calibration site 1

27

the antenna aperture A_e = .031 m^2 (-15.1 dBsm), the range R_t^2 = (3724 m)^2, the atmospheric loss L_{et} ~ 1, and the cable loss L_c = 2 (3 dB). Since the transmitter power is measured at the feed and G_t represents the ideal directive gain of the transmit antenna, the only transmit loss L_t is the aperture loss of the feed which is estimated as 1.4 (1.5 dB). The theoretical one way path loss L_{1way} is

$$L_{1way} = \frac{4\pi R_t^2 L_{et} L_c L_t}{G_t A_e F_t^2} = \frac{P_t}{P_{cal}} = 1.44 \; 10^6 \frac{L_{et}}{F_t^2} \quad (61.6 \text{ dB} + 10\log(\frac{L_{et}}{F_t^2}))$$

where 61.6 dB represents the expected power in a multipath-free lossless propagation medium.

The difference between the measured one-way losses and the theoretical loss of 61.6 dB ranged from +0.4 to +3.3 dB. The atmospheric attenuation L_{et} would be expected to be less than .1 dB over a range of only 3724 meters and contribute little to the day-to-day variations. Other factors such as pointing error of the transmit antenna or transponder horn were eliminated as a cause. During the 9/26/97 measurements, the original measurement was much lower than the -10 dBm (-18 dBm peak on the spectrum analyzer) listed. Checking the transmitter for changes, it was noted that there was moisture on the feed cover. Removing the waveguide cover and wiping the feed clear of moisture increased the measured power several dB. It was eventually concluded that most of this small time-varying difference could be attributed to small changes in L_t and a small loss in the order of 2 dB due to multipath.

The theoretical two way path loss L_{2way} is given by

$$L_{2way} = L_{1way} \left(\frac{1}{\sigma_t} \right) \left(\frac{4\pi R_r^2 L_{er}}{F_r^2} \right) \left[\left(\frac{L_{radome} \bar{L}_{col} L_{wta} \bar{L}_r}{\bar{A}_{col} N_{col}} \right) \left(\frac{\bar{L}_{comp}}{\bar{G}_r} \right) \left(\frac{L_{wtr} L_{wtp}}{\ell N_p} \right) \right] = \left(\frac{P_t}{S} \right),$$

$$L_{2way_{dB}} = 61.6 - 20.1 + 11 + 72.4 - 9.1 + 13.4 - 12 + .1 - 53.5 - 23 - 12 + 10\log(\frac{L_{er}}{F_r^2 F_t^2}),$$

$$L_{2way_{dB}} = 28.8 + 10\log(\frac{L_{er} L_{et}}{F_r^2 F_t^2}) = \left(\frac{P_t}{S} \right).$$

The difference between the theoretical lossless multipath-free estimate and the measured two way losses ranges between +0.6 and -1.6 dB. Again, given the small distance transversed by the signal, the atmospheric losses are negligibly small (< .1 dB). The height differences and ranges between the calibration site and the receiver and the site to the transmitter are similar, resulting in similar theoretical lobing positions. The similar terrain and vegetation also exist along their paths and should result in the reduction of a specular multipath component being generated near the calibrator transmitter. However, multipath does exist from scatterers near the bistatic receiver.

Furthermore, as discussed in the next section, some of these scatterers are within the main beam and high sidelobes and can cause the observed day-to-day changes.

3.3.3 Receive Site and Environment Effects

Multipath at the calibration site is not the only multipath scatter requiring consideration. Multipath near the receiver site can also provide interference that limits the system performance. For receiver mounted on an aircraft flying high above the ground, this multipath is usually limited by scatter from the aircraft structure. Even though this scatter is in the near field where the far-field antenna pattern is not in full effect, as long as the aircraft wing and other structures are not in the main beam, this scatter is usually small and can be reduced somewhat using a low sidelobe aperture weighting.

In contrast, the ground based receiver used in these measurements has nearby terrain and

Table 3.2 Propagation Measurements

	Transmitter	One-way Measurement			Bistatic Measurement		
Date	Power(pk) (dBm)	Power (dBm)	Path Loss (dB)	Diff.* (dB)	Power (dBm)	Net Loss (dB)	Difference** (dB)
8/ 6/97	56.0	-7	63	+1.4	27.8	28.2	+0.6
8/26/97	56.0	-8	64	+2.4	[1]		
9/ 9/97	54.0	-8	62	+0.4	[2]		
9/10/97	53.9	-10	63.9	+2.3	[2]		
9/25/97	55.3	-8	63.3	+1.7	28.1	27.2	-1.6
9/26/97	54.9	-10	64.9	+3.3	26.9	28.0	-0.8

* Difference between measured values and theoretical path loss value of 61.6 dB

** Difference between measured values and theoretical net loss of 28.8 dB

[1] Calibrator not used

[2] VXI hard drive failure

One Way Measurement Settings: 40 usec uncoded pulse, 500 Hz PRF
HP8559A Spectrum Analyzer, Input Attn=0 dB, Display Ref. = -10 dB, Fine = 0
dB, Resolution = 20 kHz (locked) Autotime, Cable loss = 3 dB
Bistatic processing: 16 pulse burst, 40 usec LFM waveform, 5 MHz bandwidth,
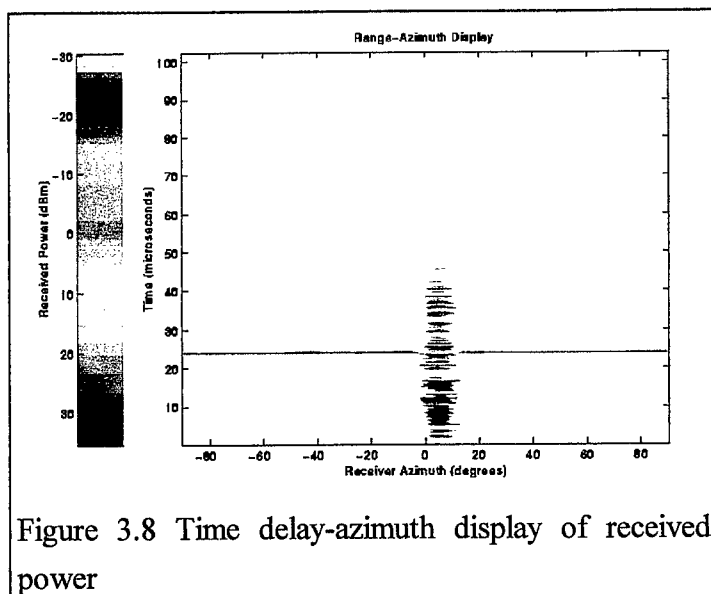uniform weighting in range, Doppler, azimuth

Figure 3.8 Time delay-azimuth display of received power

vegetation scatterers in all azimuths. When the 6 degree main beam is elevated above ground for aircraft detection measurements, the multipath scatter enters the receiver via the azimuth and elevation sidelobes that attenuate this inference significantly. However, for lookdown measurements of terrain clutter and vehicles, a depression angle of 4 to 7 degrees places the canopies of nearby trees within the main beam and places the nearby scatterers from the terrain and vegetation into the relatively high first sidelobe of the uniformly weighted elevation pattern. Therefore, when the receive beam is electronically steered away from the azimuth of the illuminated area, the multipath scatter from the trees within the mainbeam can be stronger than the energy received directly from the azimuth sidelobes.

Figure 3.8 shows the signal output in time delay (range) and azimuth space. The amplitude is color-coded and represents amplitudes ranging from -30 dBm to +35 dBm. The azimuth angle is referenced to the broadside with positive angles representing electronic scanning to the right (clockwise) and the negative angle to the left. The time delay is referenced to the beginning of the window and represents the differential time delay between the first received signal from the transmitter and the other signals. The calibrator signal is the large (red) signal located at approximately 24 microseconds and at a scan angle of +4.2 degrees. The blue regions along the same azimuth represent the sidelobes of the match filtered waveform.

The weaker signals at the same range of the calibrator are due primarily to mainbeam multipath, not due to the sidelobe response of the Taylor-weighted azimuth sidelobes. (Figure 3.9) The receiver sits atop a small hill with a large number of small trees and shrubs nearby. The depression angle of this measurement is -4 degrees, placing the tops of the small trees within the antenna's 6 degree mainbeam and placing trees, shrubs and nearby terrain within the high sidelobes.

While the displayed scan angles range from -90 degrees to +90 degrees, the element gain and aperture foreshortening limits the useful scan angles to within -50 degrees and +50 degrees

This multipath is not a problem for most of the measurements of interest because the signal from the illuminated area or target of interest is far stronger than any sidelobe response. However, this multipath does represent a problem in an operational scenario where a strong jamming source or other signal source is present.

3.3.4 Calibration Constant

The small amount of day-to-day changes indicates that the bias error of the bistatic calibrator measurement due to multipath at the town barn site is small. If small targets are measured at the location of the calibrator, no bias error exists. A measurement of the cross section of the target can be estimated by comparing the received power S_{target} with that from the calibrator [19]. This comparison is facilitated through the use of a calibration constant [35]

$$K_1 = \frac{\sigma_{cal}}{S_{cal}}$$

where the cross section of the target σ_{target} can be given as a function of the received signal power S_{cal}, $\sigma_{target} = K_1 S_{target}$.

However, most of the measurements of interest are from targets and clutter at other locations. For these measurements, the calibrator is used to create another calibration constant

$$K_2 = \left(\frac{\sigma_{cal}}{S_{cal}}\right)\left(\frac{1}{R_{r_{cal}}^2 R_{t_{cal}}^2 L_{et_{cal}} L_{er_{cal}}}\right)$$

and the target's cross section given by

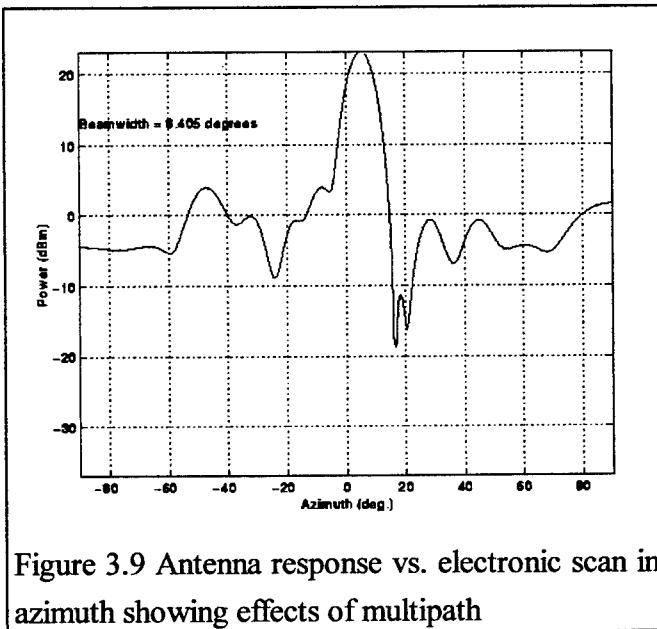$$\sigma_{target} = K_2 S_{target} R_{r_{target}}^2 R_{t_{target}}^2 L_{et_{target}} L_{er_{target}}$$

Figure 3.9 Antenna response vs. electronic scan in azimuth showing effects of multipath

where it is required that the target and the calibrator are receiving the same transmitter antenna gain and the same signal processing gain.

The error in the RCS estimates should also be estimated. Without the calibrator, an error analysis would have to be derived from equation (3.1), requiring measurements or assumptions for each value. With the calibrator, the error analysis needs to examine only the parameters given for σ_{target} in the equations given above.

31

In general, the error is a function of bias errors and random errors. For the simple case where the target is at the same position as the calibrator,

$$\sigma_{t\arg et} = \frac{S_{t\arg et}}{S_{cal}} \sigma_{cal}$$

or, in decibels,

$$\sigma_{t\arg et_{dB}} = S_{t\arg et_{dB}} - S_{cal_{dB}} + \sigma_{cal_{dB}}$$

where, for parameter σ

$$\sigma_{dB} = 10\log(\sigma).$$

The decibel representation is often used not only in the measurement of each parameter, but also in the errors that effect each parameter.

For example, the RCS of the transponder $\sigma_{cal_{dB}}$ is given by

$$\sigma_{cal_{dB}} = A_{e_{dB}} + G_{a_{dB}} + G_{dB}$$

where A_e is the aperture in the direction of the transmitter, G_a is the net gain within the transponder and G is the gain of the transponder transmit antenna in the direction of the bistatic receiver. The net gain G_a was measured to an accuracy of .1 dB and has been measured to have peak-to-peak variations of gain within +/- .5 dB after a 5 minute warm-up. If the calibrator is placed in an environment such that the temperature does not change much over the measurement period, a reasonable estimate of the mean square gain error due to drift over a measurement period of a few hours is .33 dB. Some small day-to-day changes in gain were noted, so the G_a should be remeasured before every use.

The aperture and gain of the standard gain horns are provided by the manufacturer and can be confirmed from physical measurements. The dominant random error in aperture and gain is the pointing error when using the horns. One-way experiments used to calibrate the transmitter azimuth for the calibrator location also allowed experimentation on peaking up the transponder's horns. The beamwidths of the standard gain horns are quite broad and setup by line-of-site was consistently within .5 dB of the peak aperture or gain. Again, a mean square error of .33 dB is reasonable with careful operation. Each error represents a constant but unknown bias during the measurement period. The composite error for the calibrator is the sum of the mean square errors or 1 dB.

The errors in S_{cal} and S_{target} have two types of contributors. First, the error in measuring the amplitude of S_{cal} is a function of the peak signal-to-rms noise ratios. An rms error of 1 dB requires a S/N of 18.3 dB while an error of .1 dB requires a S/N of 38.7 dB. When the received S/N from the calibrator is greater than 40 dB, this error can be ignored. The other sources of error in S_{cal} are systematic errors such as an error in the beam pointing angle of the transmitter

and receiver, a drift in the transmitter power, receiver gain or change in multipath. If the measurement of target is performed soon after the measurement of the calibrator, the error due to gain drift will be small, albeit, unknown. Similarly, if care is used to setup the beam angles, this error should also be a small, unknown quantity. Therefore, the error in measurements taken with normal care should be close to the +/- 1 dB derived for the calibrator. The measurements given in Table 3.2 tend to support this conclusion. The best method to obtained a better estimate is to make many measurements of the calibrator signal over several weeks and empirically derive the error statistics.

For the case where the calibrator is measured at one place and the target exists elsewhere, other considerations must be addressed. One is the error in range estimate. Given the stability of the system clocks used to sample range, the primary source of error in this measurement is the signal-to-noise ratio of the signal.

Another possible source of error is a difference in the multipath lobing between the target and calibration locations. For point targets not normally associated with the ground such as aircraft, this is an important consideration and must be dealt with on a case-by-case basis. However, for point or distributed targets on the ground such as trees, buildings, terrain or automobiles, the multipath lobing should be considered part of the target response.

4.0 CALIBRATION PROCEDURES FOR BACKSCATTER EXPERIMENTS

This section discusses the calibration procedures for performing backscatter measurement from point targets such as houses, towers and vehicles or distributed targets such as terrain. The general procedure for the measurement of the radar cross section of point targets requires the performance of several steps. The first section reviews the preliminary procedures for setting up the experiments. These include identifying and recording the measurement and target parameters, equalizing the bistatic receiver and measuring the calibrator return for the creation the appropriate calibration constant. Section 4.2 discusses the creation of the calibration constant and other measurement procedures for measuring the radar cross section (RCS) of point targets. Measurements of local houses and vehicles are presented as examples. Section 4.3 discusses the creation the calibration constant and other procedures for measuring the normalized radar cross section (NRCS) of distributed targets. Measurements of wooded areas, wooded hills and other areas are presented as examples. The procedures assume the use of a local transmitter with a line-of-sight view of the measurement area. The last section discusses other uses of the calibrator in attenuation measurements and related efforts.

4.1 Preliminary Procedures

The preliminary procedures prepare the system to accurately measure and identify the target of interest. After selection of measurement target, the location of the target in differential time delay and the local azimuth and elevation coordinates of the transmitter and receiver are obtained. These parameters can be confirmed by placing the calibrator at or near the target and using its measured return to center the transmit and receive beams.

Next, the measurement parameters used in the experiment are selected and recorded. These include the selection of PRF and pulse parameters that provide adequate S/N and that are consistent for an unambiguous and accurate measurement of the target. These parameters are used to define the bistatic resolution cells dimensions, the number of resolution cells within the transmit beamwidth that are calibrated within a chosen error bound and the location of these resolution cells in the receiver range-azimuth coordinates. Other parameters such as transmitter power and antenna coordinates are recorded to allow double-checks on the measurement results when surprising or unexpected results are obtained.

Equalization procedures of the receiver are then performed to create the channel compensation filters for beamforming. An earlier report discusses the equalization procedures for the bistatic system [7,35]. As discussed in Chapter 3, accurate beamforming requires the
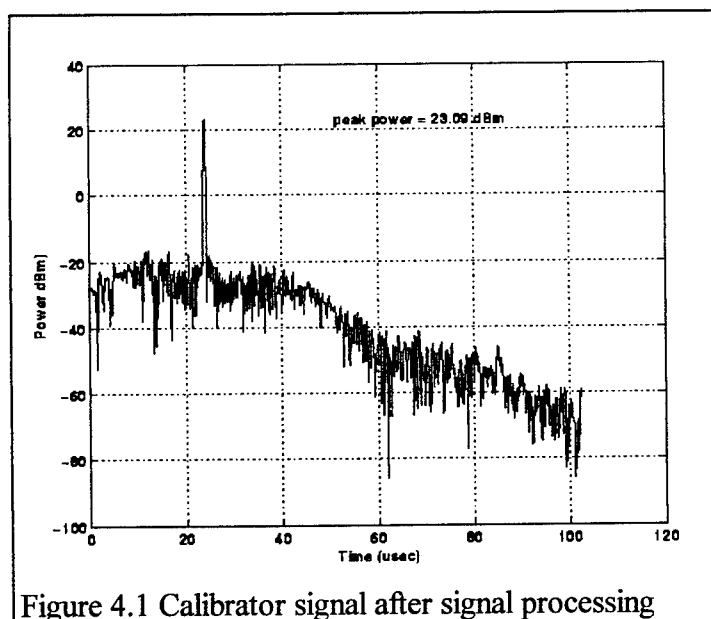
Figure 4.1 Calibrator signal after signal processing

equalization of the 16 column channels. This requires a recording of the transmit waveform using the up-converter, the down converter and the closed loop hardware in the receiver. The recording is then processed to create 16 equalization filters that compensate for the non-ideal amplitude and phase perturbations across the passband and for the difference in amplification within each channel.

The process also checks to confirm that the recorded signal amplitudes do not deviate significantly from the expected values. This check flags any drastic changes in gain or other failures within each channel before time is spent performing measurements. Over temperatures from 40°F and 70°F, the gain within each channel can change over 1 dB. After warm-up when the environmental controls keep the antenna and equipment at 68°F, the changes in gain over a period of hours are typically less than 1 dB.

Once the compensation filters are created, the system is set into the operational mode where the transmit signal is sent to the transmitter via the optical fiber link. The transmitter and receiver antennas are set at the azimuth and elevation required to illuminate and receive energy from the calibrator or other target of known cross section. The transmitter antenna is relatively narrow and must be aligned carefully to assure proper calibration. The receive antenna is broader and capable of creating multiple simultaneous beams in azimuth. While mechanically pointing the receive antenna at the target is not necessary, the receive antenna is usually mechanically steered to within 15 degrees of the target azimuth to provide full array gain in the target's direction.

The signal from the calibrator is processed using the processing planned for each target. The antenna weightings normally used are uniform and Taylor (SL=35 dB, nbar=6). The matched filter weightings commonly used are Hamming in the range domain and Hanning in the Doppler domain. Figure 4.1 presents a typical calibrator signal for the antenna beam and Doppler filter centered at the calibrator location and modulation frequency, respectively.
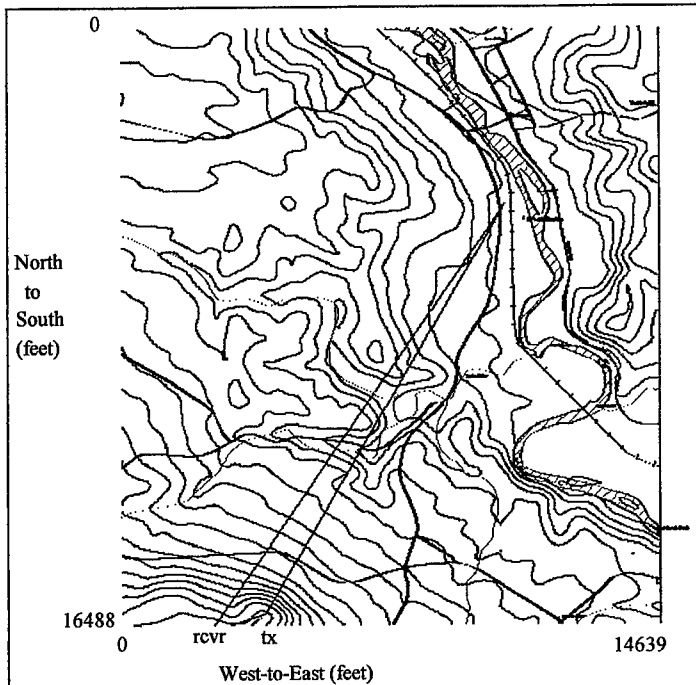
Figure 4.2 Topographic map used as a background for radar measurements

For analysis and operational presentation, a display that correlates the returns with physical features is useful. For target and clutter measurements, an appropriate background for the radar data is a topographical map that shows roads and rivers as well as terrain altitudes and, if possible, cultural and vegetation features.

Figure 4.2 shows a map used for many of the presentations given in later sections. The transmitter and receiver are located on Irish Hill. Lines from the transmitter and receiver and intersecting at the location of the calibrator are also shown. The map is oriented relative to true north.

The display of the range-angle radar data on the x-y coordinates requires a coordinate transformation. The isorange contours of a bistatic system are described by an ellipse where the foci are the transmitter and receiver locations [31].
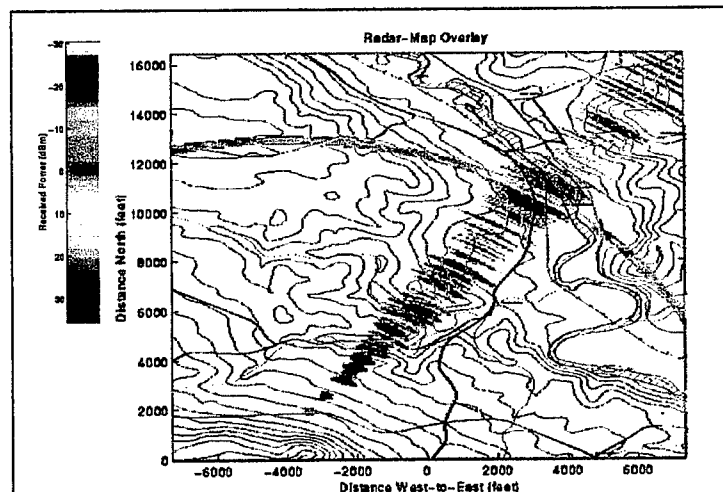
$$\frac{x^2}{a^2} + \frac{y^2}{b^2} = 1$$

where

$$a_i^2 - b_i^2 = \frac{R_{baseline}^2}{4}.$$

For a given x-y coordinate on the map, the total time delay within the data window can be given as

$$t = \frac{r_r + r_t}{c} - t_L$$

where, from geometry,

Figure 4.3 Radar display of calibrator signal over the topographic map

$$r_r = \sqrt{(x-x_r)^2 + (y-y_r)^2}$$

$$r_t = \sqrt{(x-x_t)^2 + (y-y_t)^2}$$

and t_L is the time for the energy to transit the bistatic baseline. The angle for the (x,y) point as measured at the receiver can be given as

$$angle = a\tan\left(-1 * \frac{(x-x_r)}{(y-yr)}\right) + \theta_{scan}$$

where θ_{scan} is the angle of the beam relative to true north and atan corresponds to the arc tangent.

The mapping from polar to rectangular coordinates is limited to within 90 degrees of the broadside azimuth. Areas corresponding to other angles are given as white or other default color. The propagation time for the signal to transit the baseline is ~1.6 microseconds. Most of the other delays in the system are the delay in the fiber optic line between the receiver shelter and the transmitter and the delays in the up-converter and down-converter .

Figure 4.3 shows the radar display superimposed on the terrain map shown in Figure 4.2. The strong return from the calibrator is located near the road passing the Newport town barn. The elliptical band caused by the mainbeam multipath discussed in Chapter 3 is evident. The band appears more circular because the terrain map dimensions were distorted to fit the rectangular format of the radar display. The weak range sidelobe responses are also evident.

Figure 4.4 presents a range-Doppler display of the illuminated area around the calibrator. The calibrator signal is the strong (red) signal in the center Doppler filter while the first Doppler filter on the far left side shows the returns from the nearby town barn, houses and vegetation.This display allows the examination of the relative clutter and target amplitudes. The Doppler estimate in this figure was created using only 16 pulses. With a larger number of pulses taken over a longer time history, the display allows the analysis of the difference in the clutter spectra as a function of range or the detection of screened targets in the midst of vegetation clutter.

Figure 4.5 presents a range-azimuth presentation of the output of Doppler filter 1 that is centered at 0 Hz. The large return just beyond the calibrator position is from the large town barn while the return from across the road from the calibrator is from residential homes. The effects of mainbeam multipath is apparent in the low-level amplitudes spread in azimuth. The depression angle of the transmitter ϕ_{dt} was -4.5 degrees and the extent of the transmitter 2 degree beam on the ground near the calibrator is about 5500 feet long. This explains the extent of the strong

Figure 4.4 Range-Doppler display of illuminated area around the calibrator
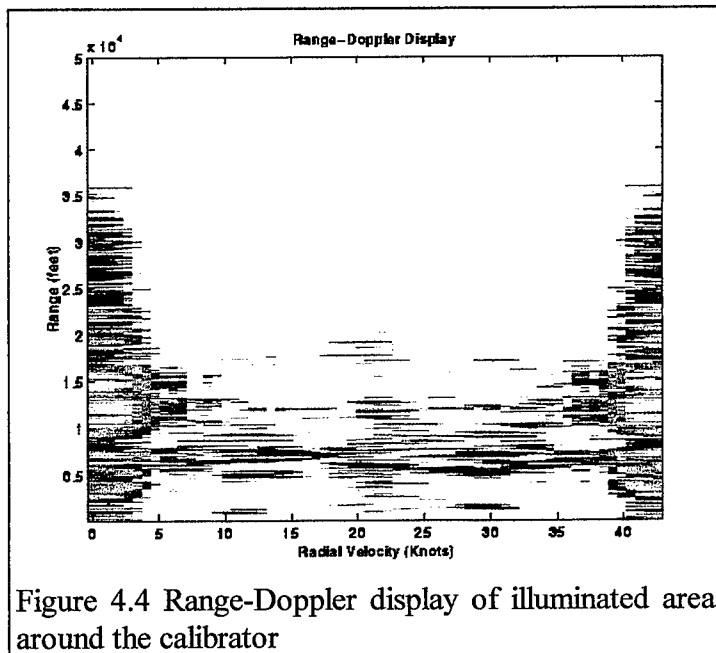
returns from the terrain and structures within about 2500 feet of the calibrator. The large nearer returns at 7000 feet north, 1000 feet east are from large structures located on a ridge. The next step is the creation of the calibration constant appropriate for relating received power to radar cross section.

Figure 4.5 Clutter display from the zero Doppler filter
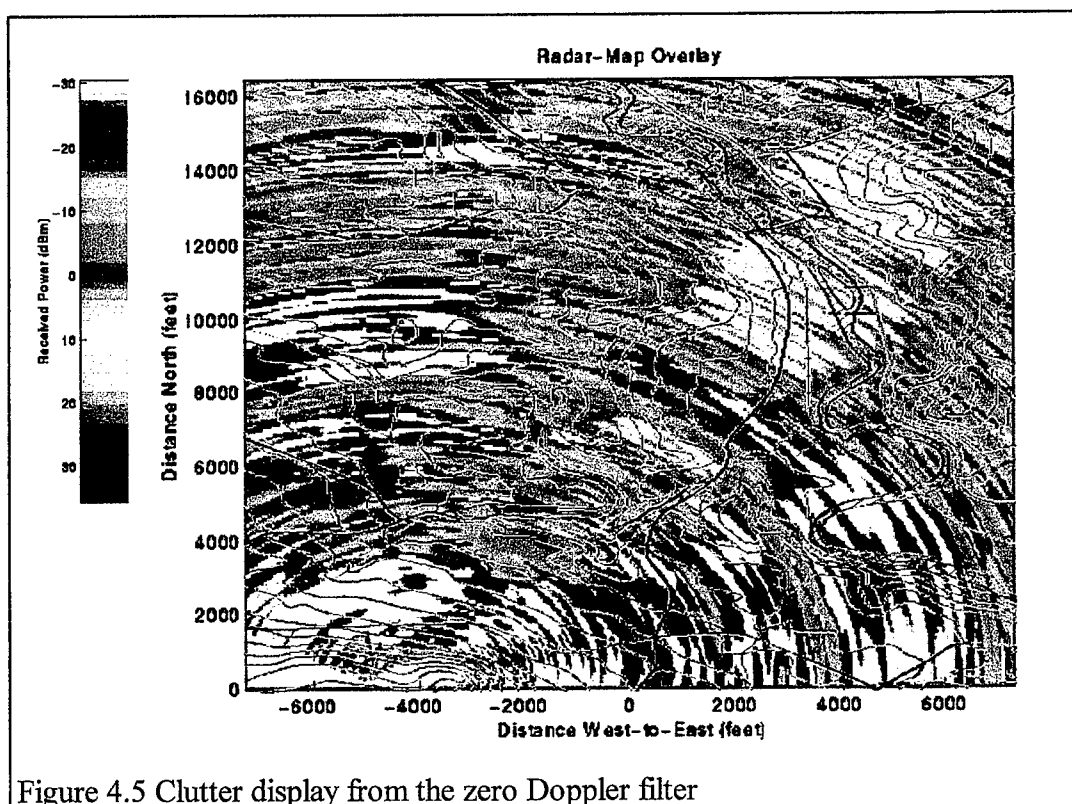
4.2 Point Targets

After the preliminary measurements are performed and the calibrator signal has been recorded, the next step is to compute the calibration constant for use in the target and clutter measurements. The calibration constant is given as

$$K_2 = \left(\frac{\sigma_{cal}}{S_{cal}}\right)\left(\frac{1}{R_{r_{cal}}^2 R_{t_{cal}}^2 L_{et_{cal}} L_{er_{cal}}}\right)$$

For the measurement given in the previous section, S_{cal} = 204.2 mw (23.1 dBm), σ_{cal} = 102.3 square meters (20.1 dBsm), R_{rcal} = 13635 feet (41.3 dBft) and R_{tcal} = 12215 feet (40.9 dBft). The range is measured in feet for this discussion because the ranges are short and the background map used is dimensioned in feet. Also, over the short ranges to the calibrator and the target areas, L_{ercal} and L_{etcal} have very small values and can be ignored. Therefore,
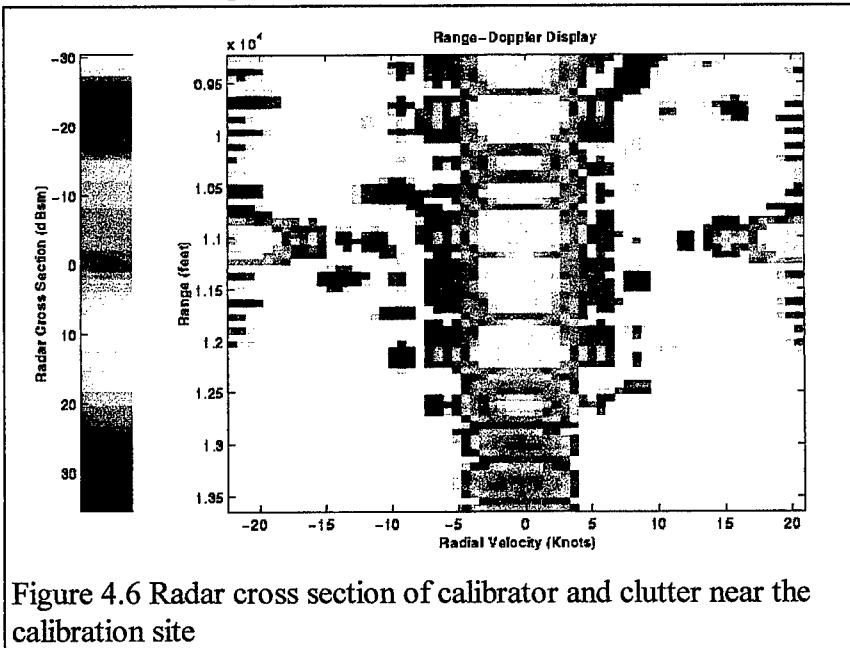
$$K_2 = \left(\frac{102.3}{204.2}\right)\left(\frac{1}{(13635)^2(12215)^2}\right) = 1.81x10^{-17}$$

$$K_{2_{dB}} = -167.4 \text{ dBsm} / \text{mw - ft}^4$$

The radar cross section of a return can now be given as

$$\sigma_{target} = K_2 S_{target} R_{r_{target}}^2 R_{t_{target}}^2 .$$

Figure 4.6 shows a range-Doppler plot of the calibrator and the town barn area after modification by the calibration constant. The range given represents the range within the recording window and does not include the window delay. The signal processing parameters used to create this output was the same as that used to create the calibration constant. The waveform was 40 usec pusle modulated with a linear frequency modulation of 5 MHz bandwidth. The pulse matched filter used a Hamming weighting. The Doppler processing used a 16 pulse burst and Hanning weighting. Interpolation was provided using 64 point FFT.

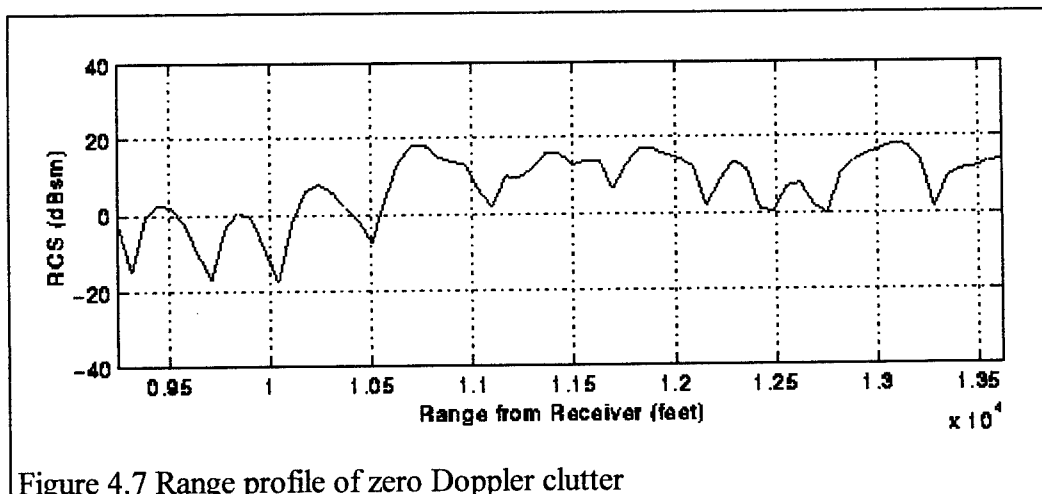Figure 4.6 Radar cross section of calibrator and clutter near the calibration site

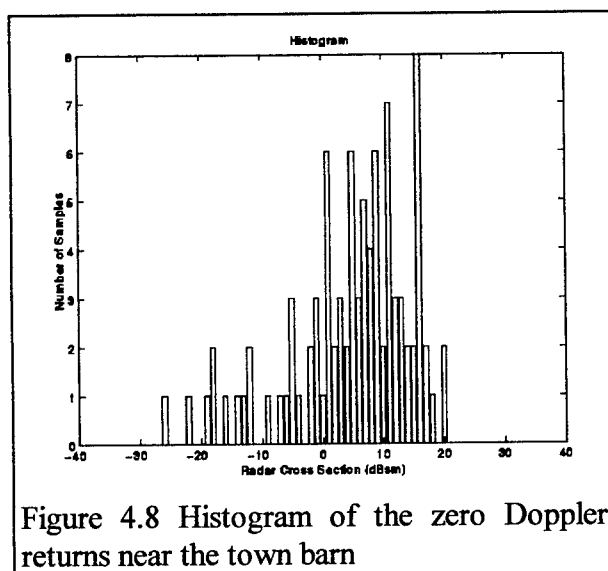Figure 4.7 Range profile of zero Doppler clutter

Figure 4.8 Histogram of the zero Doppler returns near the town barn

The calibrator radar cross section of 20.1 dBsm is shown at -22.5 knots while the RCS of the clutter is centered at zero knots. Figure 4.7 shows the range profile of the clutter returns. The clutter backscatter is dominated by the houses and other manmade structures that provide a far larger backscatter that the terrain and vegetation. The quasi-periodic structure in the clutter return versus range is due to the spacing of the structures.

Figure 4.8 presents a histogram of the estimated RCS values. The stronger returns over 0 dBsm are caused primarily by the buildings while the weaker returns are associated with the relatively flat terrain and vegetation before the buildings. The town barn located at 11500 feet is oriented such that it does not provide a specular return. Therefore, even though it is a large building, it presents less bistatic radar cross (~16 dBsm) than its size might indicate. Similarly, the other houses are also oriented such that the radar is looking at their corner view instead of their broadside view.

Table 4.1 lists the parameters of the other point target examples presented in this section. The same LFM waveform was used in all measurements and low sidelobe weightings were used in the range and Doppler domains to reduce interference from strong scatters and to minimize any ambiguity in interpreting the outputs. For many of the measurements, Doppler filtering without MTI provided sufficient attenuation to see stronger moving targets. However, when it was

40

Table 4.1 Parameters in measurements of point targets

Target Description	Range from rec. (feet)	Depression angles Tx (deg)	Depression angles Rec. (deg)	Bistatic Angle (deg)	Number of pulses	Number of cells	Mean RCS (dBsm)	Median RCS (dBsm)
Town Barn	12215	4.5	4.0	5	16	45	11.1	6.7
Farm	4500	4.6	5.1	27	16	18	1.9	0.0
Village	16370	3.4	3.5	3	16	62	13.2	7.1
Auto	12000	4.5	4.0	5	34*	45	N/A	N/A

Azimuth wt: Taylor, 35 dB sidelobe, nbar=6
Waveform: LFM, 5 MHz bandwidth, 40 microseconds, Hamming weighting on receive
Doppler filter: Hanning weighting, interpolation using 64 point FFT
* 3 pulse MTI preceded the 32 pulse Doppler filter

desired to push the time-varying clutter residue in the non-zero Doppler filters below the thermal noise, the use of a three pulse MTI canceller before the Doppler filters was necessary.

The town barn example used the same azimuth and elevation parameters as the calibrator, requiring only compensation in range. Figure 4.9 presents an example of using the calibrator measurement at one location to perform measurements of targets at another location. The target in this case was a farm with a large farm house, barn, silo and other smaller structures.

The measurements were performed after the town barn measurements and used the same
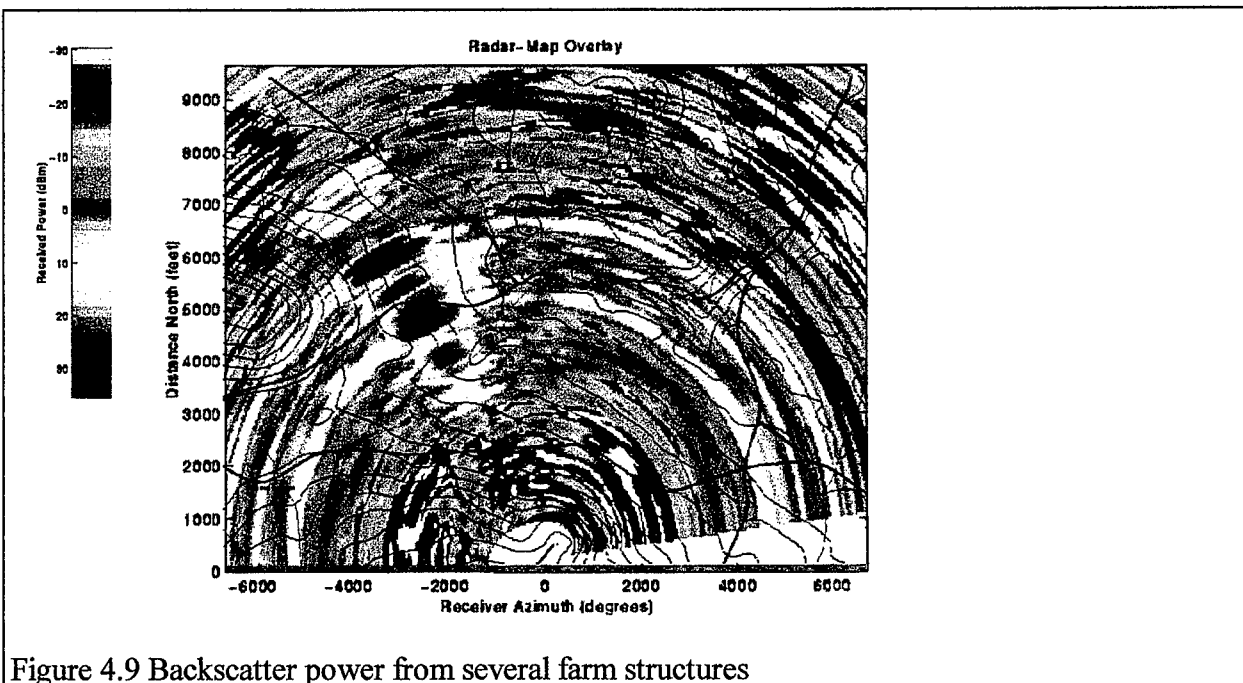

Figure 4.9 Backscatter power from several farm structures

calibration constant. The transmitter antenna was set at an azimuth and elevation to place the farm structures at beam center. Measurements were performed using the same parameters as the town barn measurement. The intended illuminated area in Figure 4.9 is an area on the south side of Newport road centered about 5000 feet north by 2400 feet west. Figure 4.10 presents a range profile of the received power as well as the radar cross section. Again, none of the buildings were oriented to provide a strong specular return and the estimated radar cross sections are comparable to those observed for the houses in the previous example. Figure 4.11 shows the power received from the village of Newport. Most of the business section of this village is screened by tree and nearer buildings. Most of the directly illuminated portions contained residential structures or small commercial buildings.

Figure 4.12 presents the range profile and RCS for the returns in the zero Doppler filter. Once again, the magnitude of the clutter from the town is similar to the RCS previously measured for houses. Figure 4.13 provides a histogram of the radar cross section estimates. The mean and shape of the histogram are similar to the town barn area. Figure 4.14 presents a range-Doppler plot of the returns. In addition to the zero Doppler returns, signals in other Doppler bins can also be observed. These signal represent scatter from moving targets such as vehicles or birds and can represent weak scatterer in the main beam or stronger scatterers moving in the transmitter
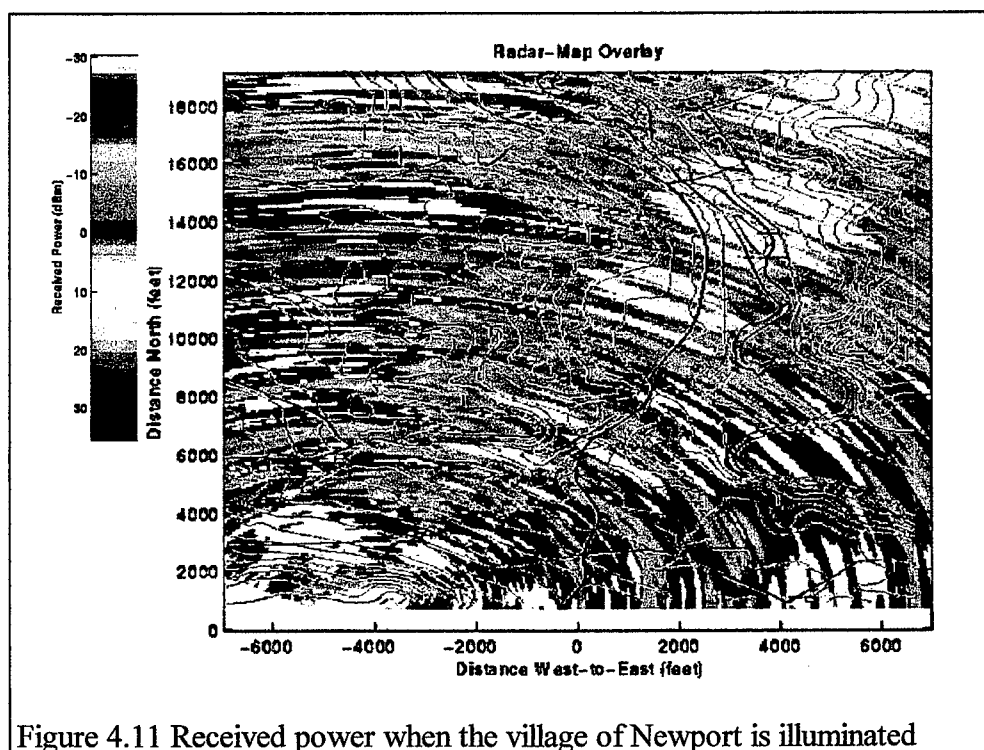

Figure 4.11 Received power when the village of Newport is illuminated
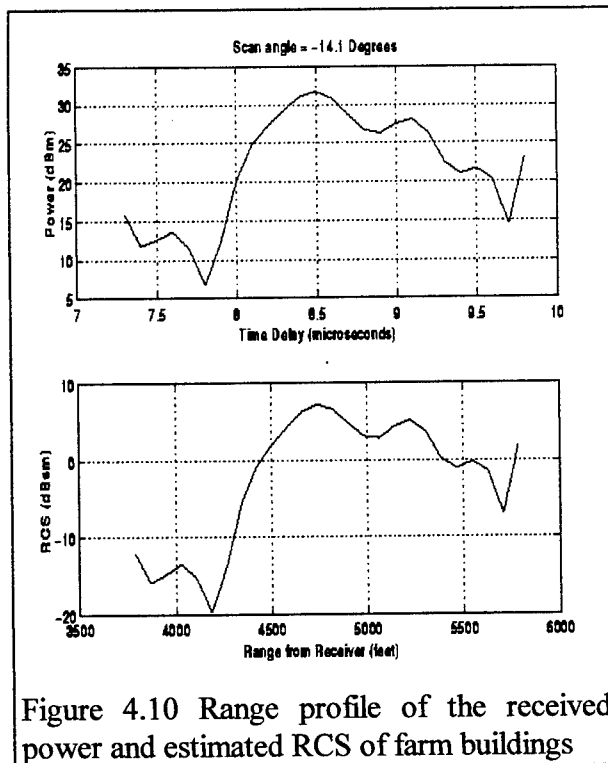
Figure 4.10 Range profile of the received power and estimated RCS of farm buildings
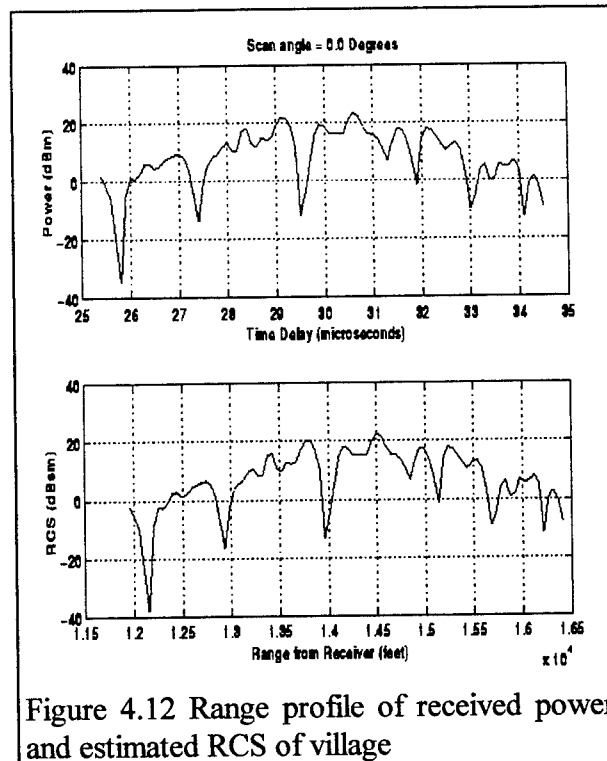

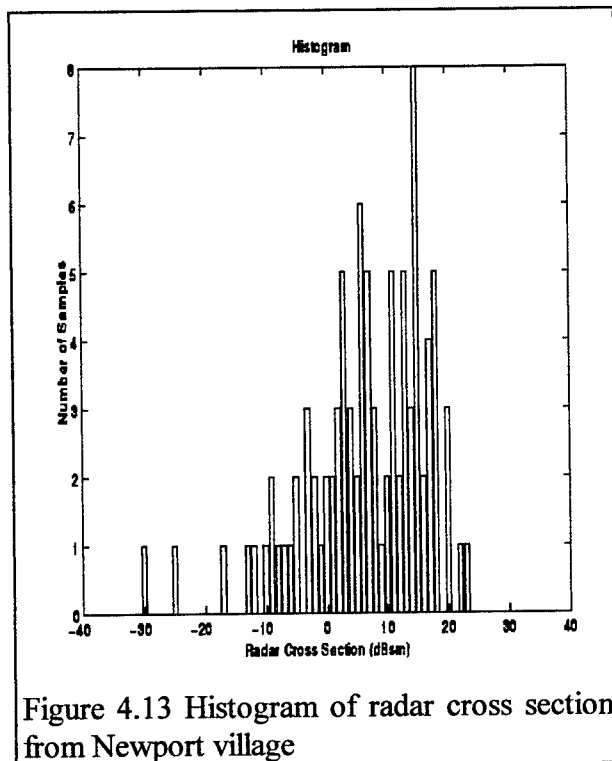Figure 4.12 Range profile of received power and estimated RCS of village

Figure 4.13 Histogram of radar cross section from Newport village

or receiver sidelobes. Bistatic scatter from vehicles represents another important area of interest both as a source of clutter and as a desired target. One relatively strong return is observed at a range of approximately 14000 feet and 20 knots. With a radar cross section in the order of 1 square meter, this return is probably from a vehicle. Figure 4.15 presents the 20 knot filter output overlaid on the topographic map. The return correlates well with the main road through the village and is probably scatter from a vehicle of unknown make or model.

Radar cross section measurements of a passenger vehicle were performed to illustrate how such measurement can be performed. The vehicle was a 1989 Honda Accord. The vehicle was driven near the calibration site at a constant
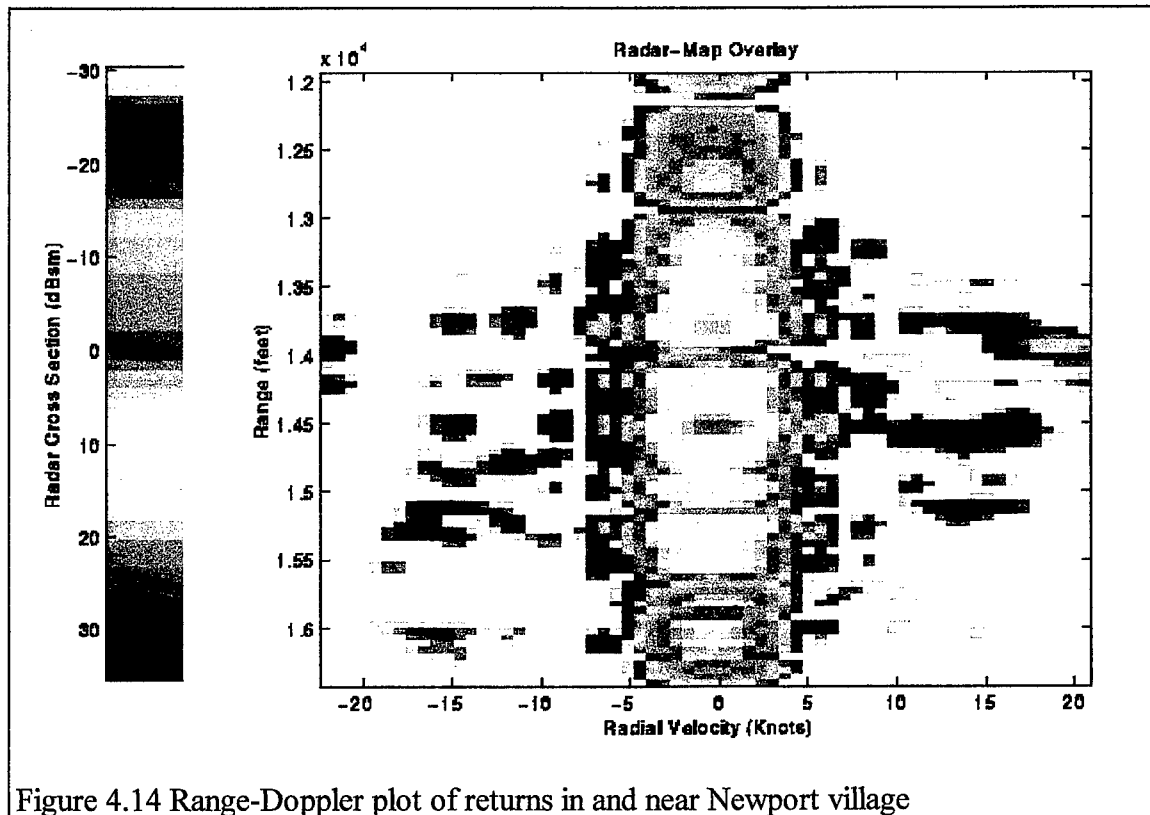
43

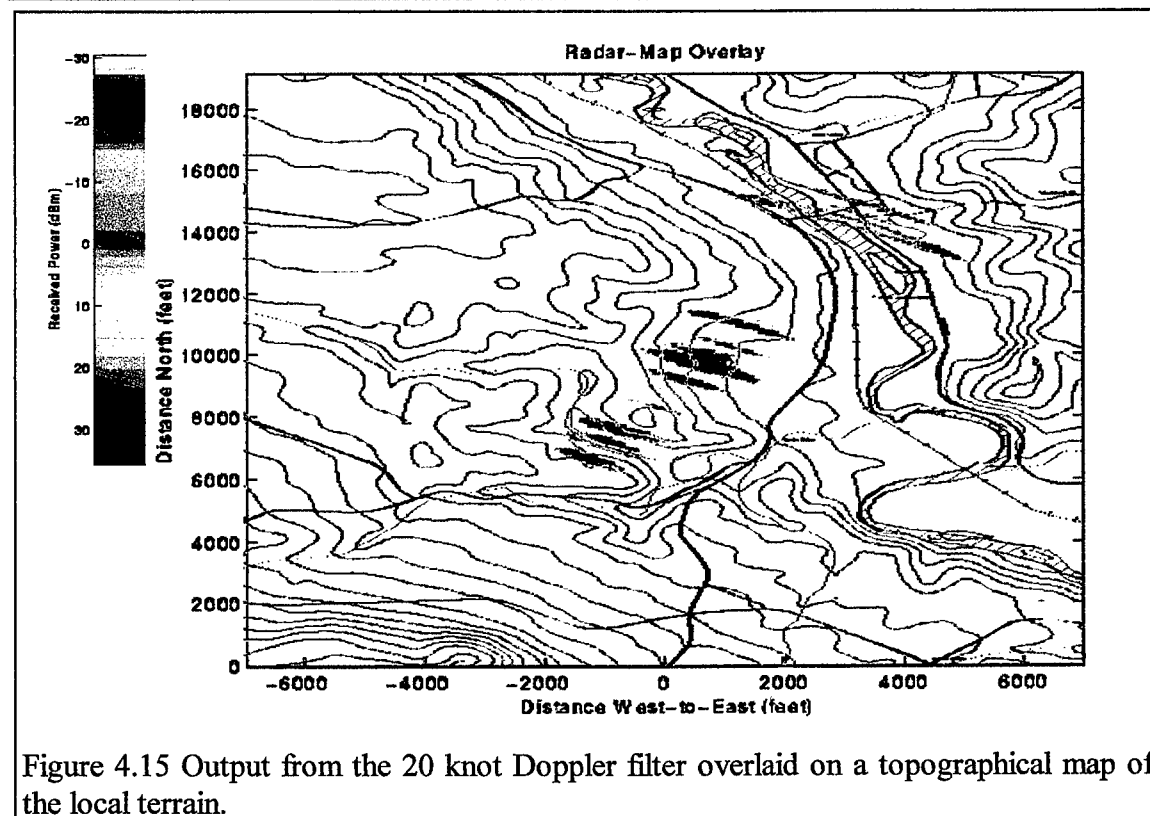Figure 4.14 Range-Doppler plot of returns in and near Newport village

Figure 4.15 Output from the 20 knot Doppler filter overlaid on a topographical map of the local terrain.

speed of 30 mph or 26 knots. When other vehicles also entered the measurement area, their characteristics were also noted.

Figure 4.16 presents the results of a measurement with the test vehicle travelling away from the site toward the village of Newport. The processing used in this measurement differs from that used for stationary clutter. First, a three-pulse MTI canceller was used before the 32-pulse Doppler filter to provide more attenuation of the stationary clutter. Second, the response of a three-pulse canceller is

$$(f) = \frac{16}{\sqrt{6}} \left(\sin(\frac{\pi f_d}{PRF}) \right)^2$$

where normalized binomial weights of $\left[\frac{1}{\sqrt{6}} \frac{2}{\sqrt{6}} \frac{1}{\sqrt{6}} \right]$ are used to provide unity noise gain. To provide a display where one calibration constant is used for all moving targets, a compensation filter of

$$|H_c(f)| = \left(\sin(\frac{\pi f_d}{PRF}) \right)^{-2}$$

is applied to all filters except the zero Doppler filter, resulting in a sharp discontinuity around 0 knots.
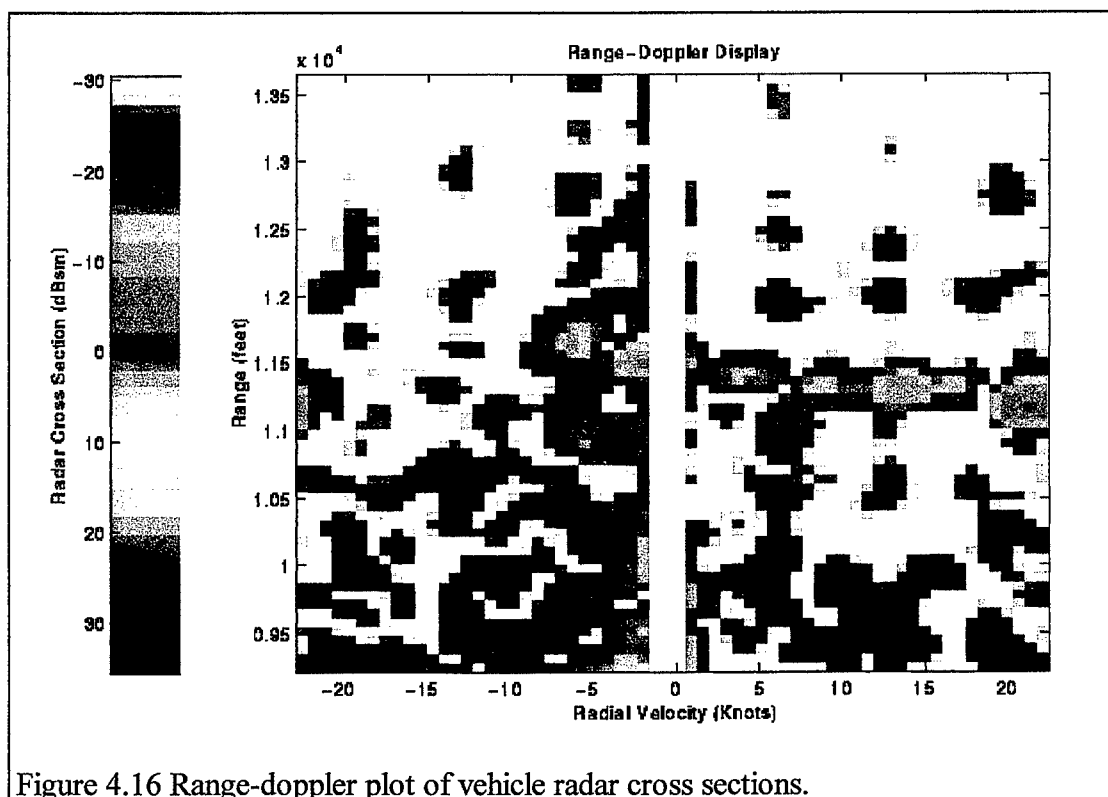

Figure 4.16 Range-doppler plot of vehicle radar cross sections.

The returns from at least two vehicles are shown in the image. The primary return from the test vehicle is located at ~11200 feet and +22 knots. Note that the velocity response is ambiguous for velocities exceeding 22.5 knots. Therefore, a vehicle traveling at a radial velocity of -26 knots would show up as +19 knots on this display. Figure 4.2 shows that, near the calibration site, the road is nearly parallel with the bistatic bisector and the radial velocity is close to the true speed of the vehicle. Figure 4.17 presents the Doppler profile of this range cell. The estimated radar cross section of the test vehicle is -0.5 dBsm.

The next strongest return is located at +15 knots and is from a small pickup traveling away from town and toward the radar. The return from this vehicle has an estimated radar cross section of -5.5 dBsm. Most of the returns near the zero Doppler filter represent the response of the adjacent filters (centered at -0.7 knots and +0.7 knots) to the ground clutter. The other stronger responses are similar to other multipath responses of moving targets in the midst of large stationary scatterers that has been noted in other measurement efforts. [19].

This multipath phenomenon is further presented in Figures 4.18 and 4.19 where only the test vehicle is in the beam. In this case, the vehicle is moving away from the village and was recorded when it passed the town barn near the calibration site. The direct return from the vehicle is located at -21 knots. No other vehicle or other sizable moving scatterer is moving within 350 feet of this vehicle.

The relatively strong returns just beyond the vehicle range at -18 knots, -14 knots, -7 knots and +9 knots are multipath returns from the nearby structures. While these returns at -10 to -15 dBsm are 5 to 10 dB weaker that the main response, they may be useful in the detection and intelligence analysis associated with operational systems[19].
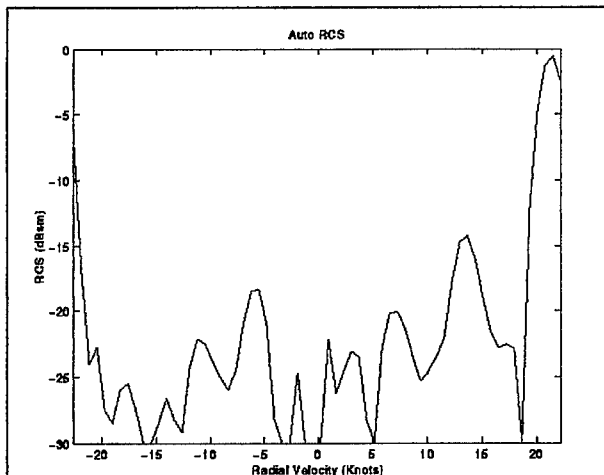
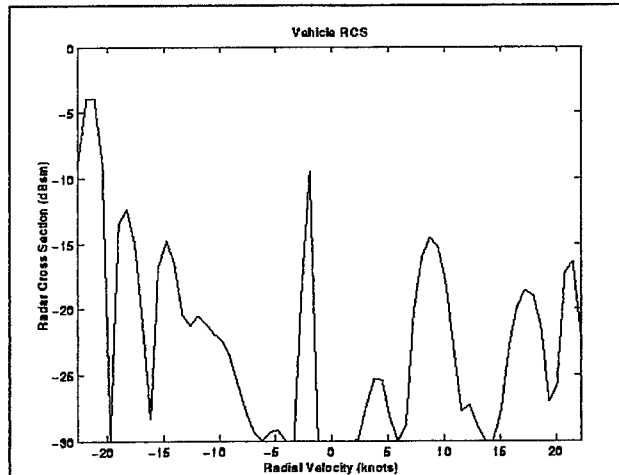Figure 4.17 Doppler profile of response from a small pickup truck

Figure 4.19 Doppler profile of the range cell containing the test vehicle response.
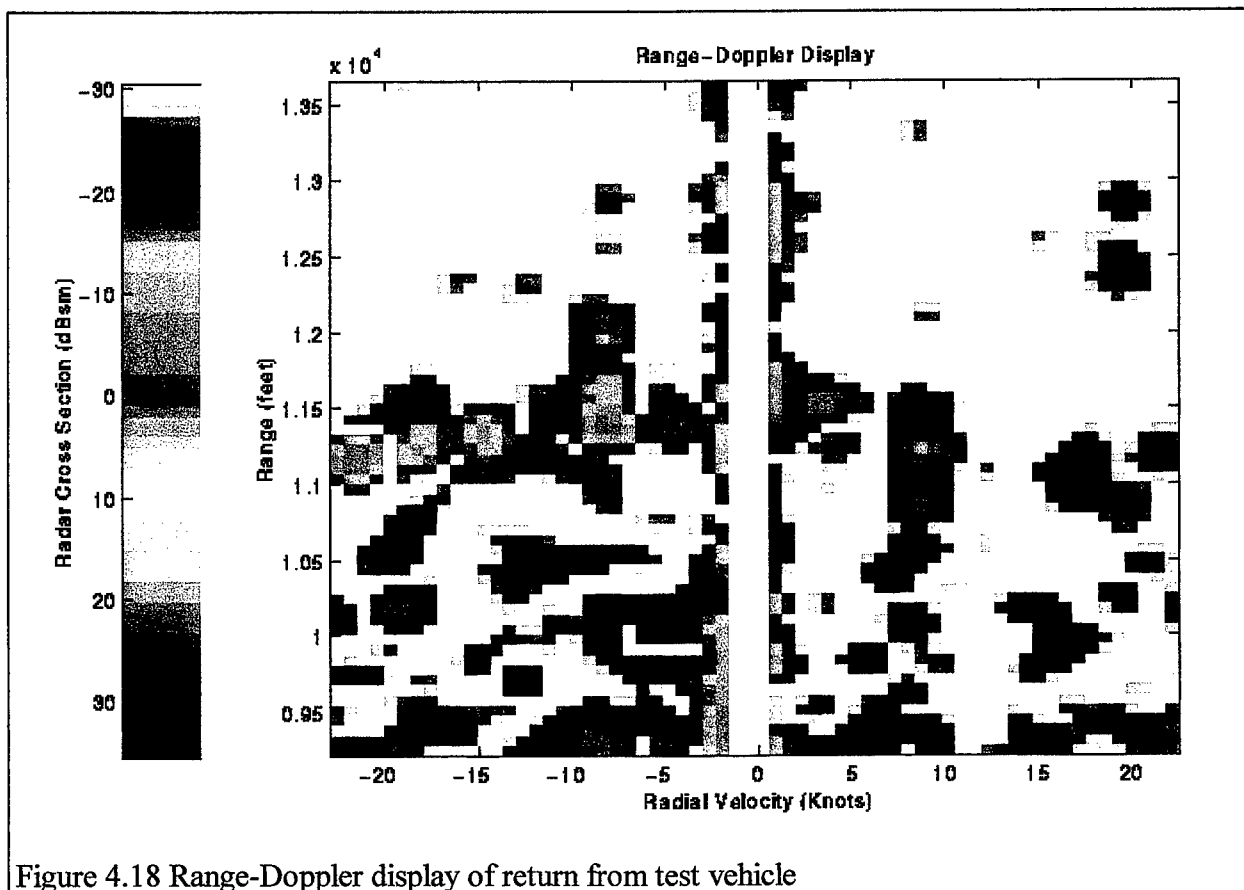

Figure 4.18 Range-Doppler display of return from test vehicle

4.3 Distributed Targets

The normalized cross section of distributed targets can be given as

$$NRCS = \frac{\sigma_{target}}{A}$$

where A is the bistatic resolution cell. Figure 4.20 shows the bistatic resolution cell and other geometric parameters. The transmit antenna is a 10 foot dish and provides a beamwidth of 2 degrees at S-Band. This beamwidth is far narrower than the receiver's beamwidth that can range from 5.6 degrees (uniform weighting) to 8.0 degrees (low sidelobe weighting). With the transmitter on the same hill only a short distance from the receiver, most of the measurements are pseudo-monostatic with the distance from the target to the transmitter approximately equal to the distance from the target to the receiver.

Therefore, for the bistatic angles and ranges used in this discussion, the bistatic resolution cell is bounded by the transmitter effective beamwidth and the waveform's effective pulse width

$$A \sim \frac{c\tau}{2\cos(\beta/2)} \frac{R\theta_e}{\cos(\beta/2)}$$

where β is the bistatic angle. For the LFM waveform, the effective pulse width τ is well approximated by the -3 dB pulse width of the compressed pulse. Similarly, the effective beamwidth of the transmit antenna is close to the -3 dB beamwidth of the transmit antenna.

The procedure for performing measurements of NRCS is similar to that for measuring RCS of point targets discussed in section 4.2. The same calibration constant as used for RCS is

Figure 4.20 Bistatic resolution cell
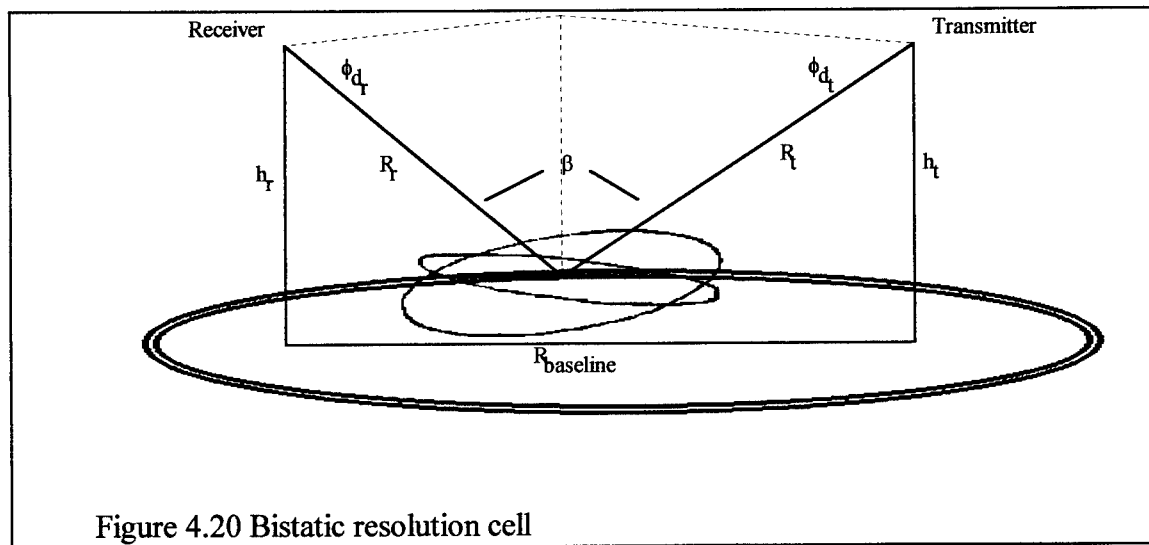
computed for each measurement. The only additional steps are the calculation of the resolution cell area for each sample and the division of the estimated radar cross section by this area.

Measurements of several clutter areas were performed during the 1997 tests to establish the measurement procedures and to provide useful measurements of the local environment. One limitation of the current test system at Newport is the manual use of the narrow transmit beam. Measurements of distributed clutter are usually statistical in nature and require many samples from a similar areas to provide statistical significance. The use of a narrow transmit beamwidth requires stepping the beam in azimuth to get the hundreds of independent range cells desired, especially at high depression angles. The manual control of the antenna and the limited recording capability available in 1997 limited the measurements to the number of samples that could be recorded. For the examples presented here, only the number of range cells within one transmitter beam position was used. Table 4.2 lists the parameters of each measurement area including the number of resolution cells within the transmit antenna 1 dB beamwidth. In general, the number of samples within the 1 dB beamwidth was too small to obtain more than first order statistics of the density function. Therefore, only the median and the mean values were obtained. In all of the measurements, the calibrator site used was the same site near the town barn that was use in the point clutter measurements.

Table 4.2 System parameters of the distributed clutter measurements

Target Description	Distance From Recr (feet)	Depr. Angles Trans (deg)	Recr (deg)	Bistatic Angle (deg)	Resoln Cells	Mean NRCS	Median NRCS
Forest	4497	8.0	7.8	36	7	-25.3	-27.0
Forest	6000	6.0	6.0	26	14	-22.4	-29.6
Forest	9840	4.0	3.7	11	30	-24.2	-26.2
Wooded Hills	18748	2.0	1.6	6	179	-25.8	-30.0
Golf Course	13438	3.4	2.4	13.6	87	-27.6	-32.4

4.3.1 Forest

A forest dominated by mature sugar maple and birch trees exists just below Irish Hill and extends for several miles to the west of Newport village. The forest is similar to that found throughout the northeast US as well as Europe. The extent of the forest provides an opportunity to measure the backscatter as a function of depression angle. The angles chosen in this demonstration are 8 degrees, 6 degrees and 4 degrees.
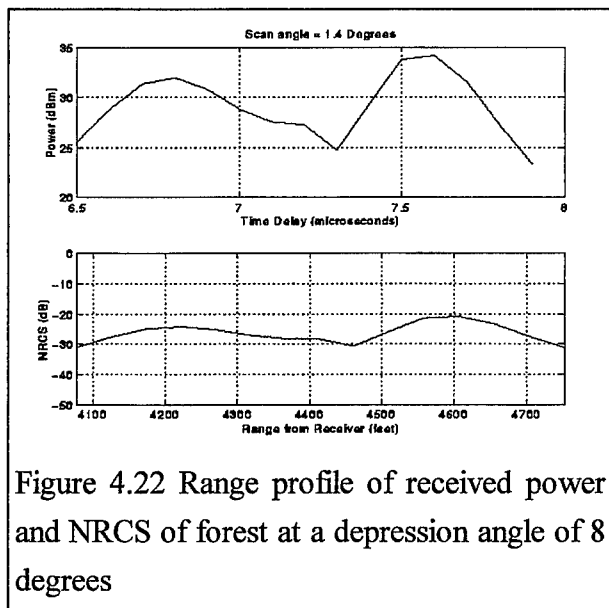
Figure 4.22 Range profile of received power and NRCS of forest at a depression angle of 8 degrees
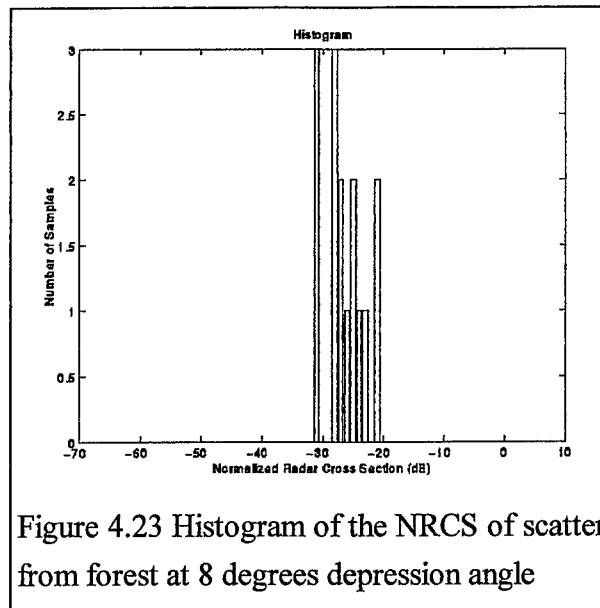

Figure 4.23 Histogram of the NRCS of scatter from forest at 8 degrees depression angle

Figure 4.21 shows the illuminated area when the transmitter antenna depression angle is at 8 degrees. The area of interest is the nearest patch of strong clutter which starts at a boundary between the forest and a field and extends north into the forest. Because of the high depression angle and the short range, only 7 range cells are contained within the transmitter's 3 dB beamwidth. Figure 4.22 shows the range profile of the received power and estimated normalized radar cross section. The front edge of the forest is near 4200 feet where the signal reaches a minor peak. A higher peak is reached after a small break in the forest. Figure 4.23 presents a histogram of the NRCS values.
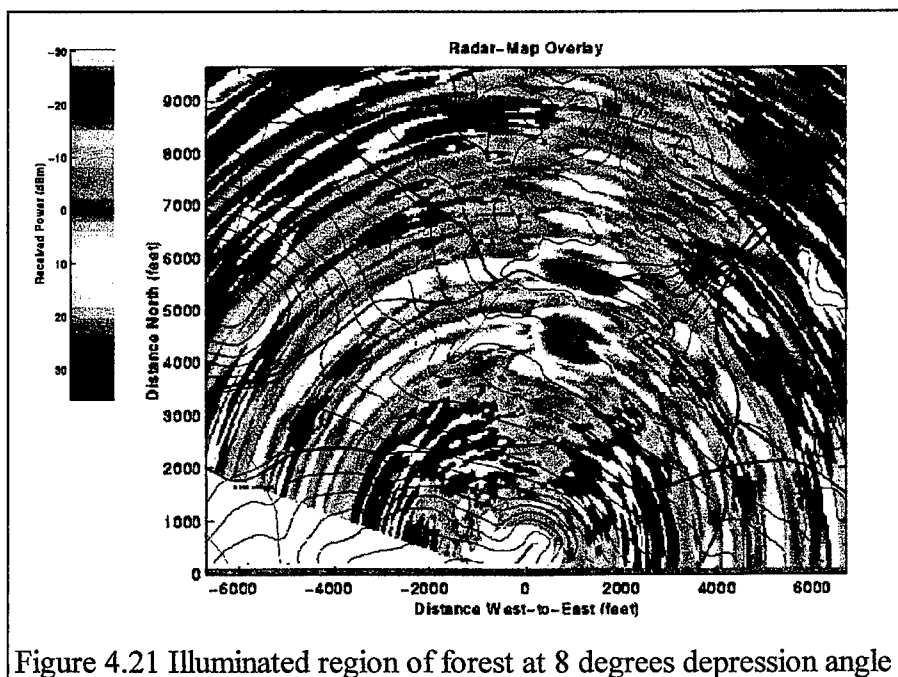

Figure 4.21 Illuminated region of forest at 8 degrees depression angle
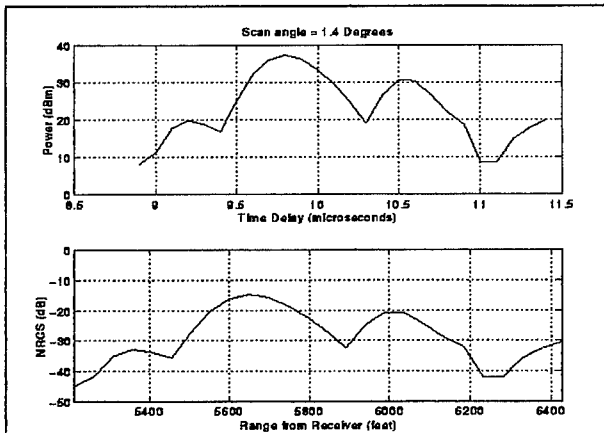
50

Figure 4.25 Range profile of received power and NRCS of forest at a depression angle of 6 degrees
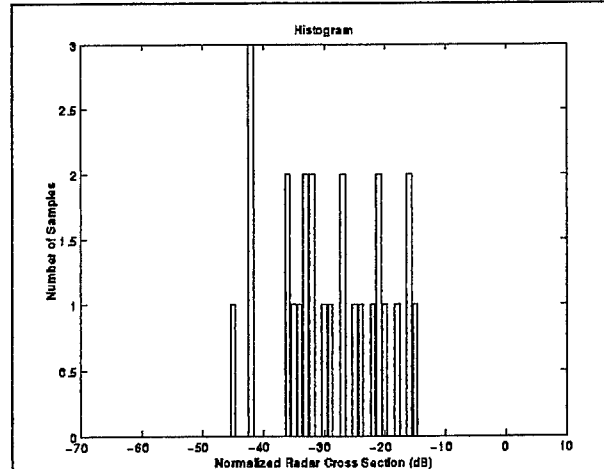

Figure 4.26 Histogram of the NRCS of scatter from forest at 6 degree depression angle

Figure 4.24 presents the clutter power from the forest at 6 degree depression angle. The area of interest is the area just north of Newport road. Two factors distinguish this area from the previous forest area. First, the road is lower than the ground level of the forest, exposing more terrain and tree trunks to the radar illumination. Second, this area of the forest rises in elevation above the road to a small ridge which also has the effect of presenting more scatterers per resolution cell. The ridge also provides a some degree of shadowing for the forest area on the north side of the ridge, reducing the illuminated power and the subsequent backscatter.

The range profiles shown in Figure 4.25 show the strong near side of the ridge, following by a reduction in signal from the shadowed area and an increase in scatter as the ridge's shadowing effect tapers off with range. Another effect of the ridge and shadowing is to increase the spread in the NRCS density function as shown in Figure 4.26.
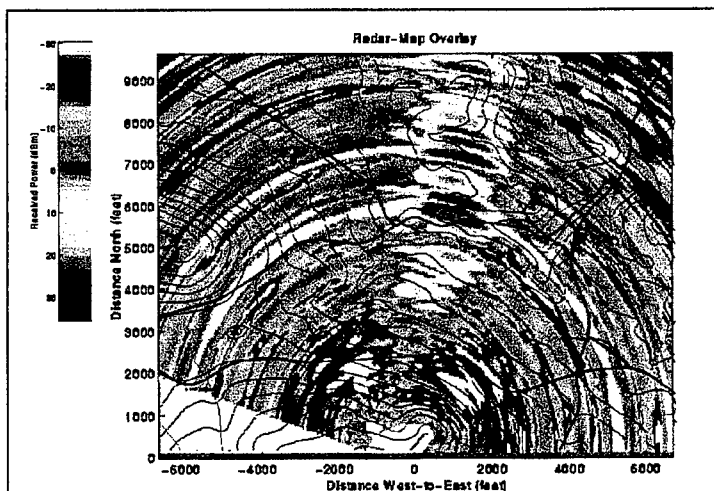
Figure 4.24 Illuminated region of forest at a 6 degree depression angle

Figure 4.28 Range profile of received power and NRCS of forest at 4 degrees depression angle

Figure 4.29 Histogram of the NRCS of scatter from forest at 4 degrees depression angle
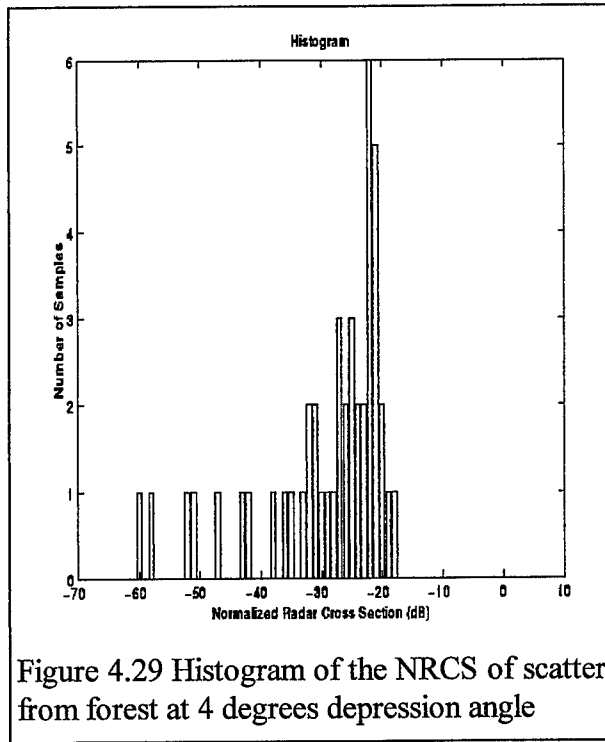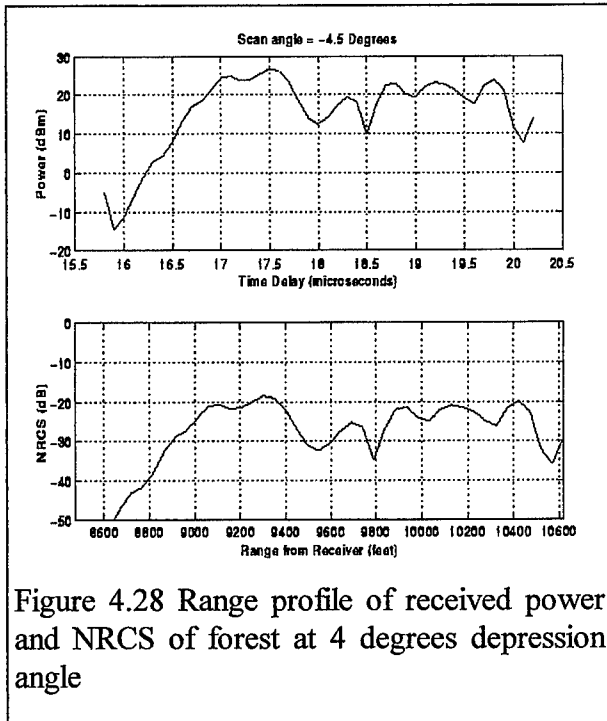
Figure 4.27 shows the measurement from forest at a depression angle of 4 degrees. At this angle, the number of range cells within the 1 dB beamwidth of the transmitter has increased to 30 cells. This forest region covered terrain of relatively constant altitude, resulting in little shadowing. This is reflected the relatively consistent amplitudes between the ranges of 9000 feet and 10500 feet. It is also reflected in the narrow histogram and the small difference in the measured mean and median values.
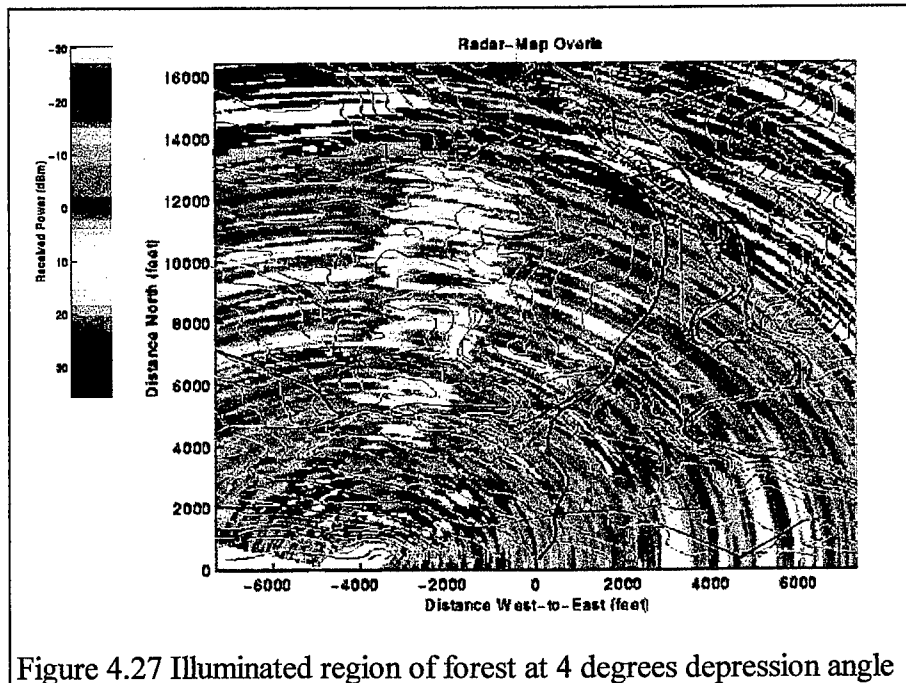
Figure 4.27 Illuminated region of forest at 4 degrees depression angle

52

Figure 4.31 Range profile of received power and NRCS for a local golf course

Figure 4.32 Histogram of the NRCS of scatter from a local golf course
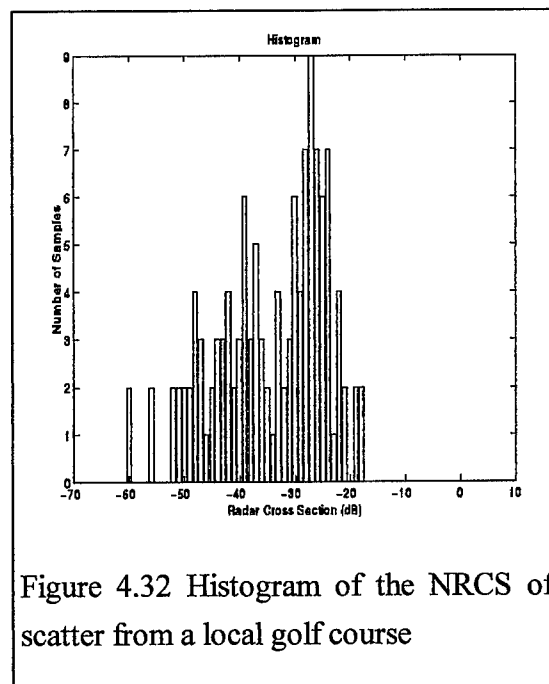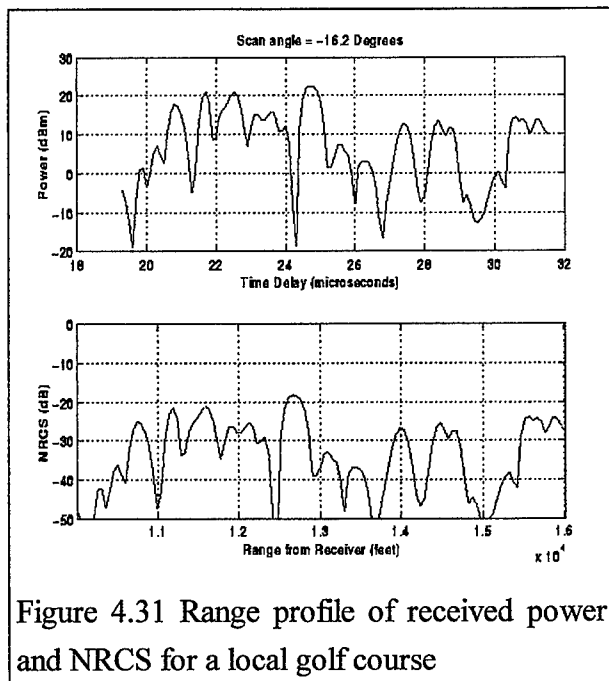
4.3.2 Golf Course

The golf course was chosen as an example of a non-natural area mixing large open spaces which provide low backscatter and areas of trees and hedges with provides a high backscatter.

Figure 4.30 Power received from a local golf course (3.4 degrees depression angle)
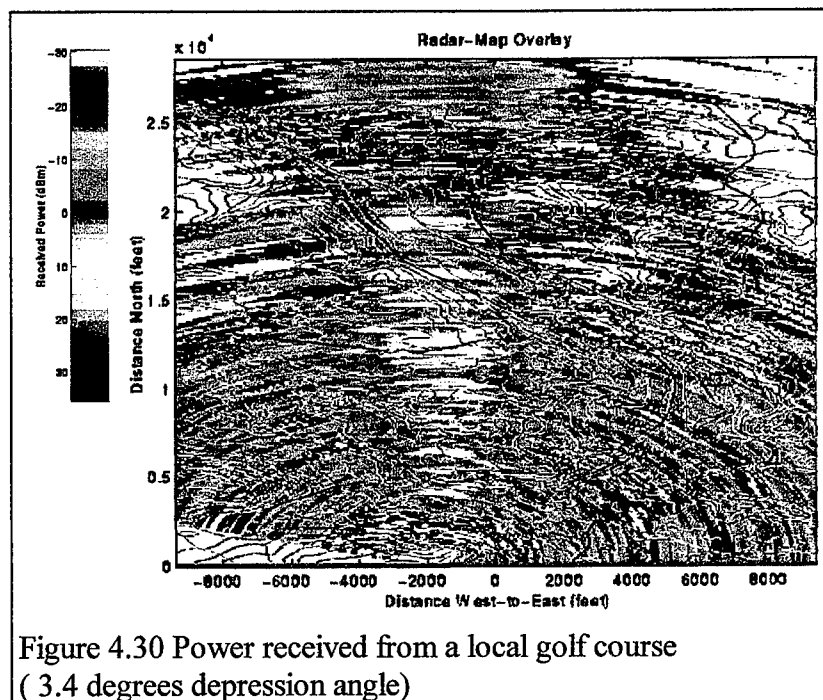
The histogram shown in Figure 4.32 shows the wide spread in the NRCS while Figure 4.31 shows a rapid fluctuation in range, implying a short correlation length. The stronger returns that are from the trees at the tree-fairway boundaries, are comparable to the returns from deeper forests. This indicates that the strongest returns are from boundary regions where the numbers of unshadowed or unscreened scatterers are higher.

53
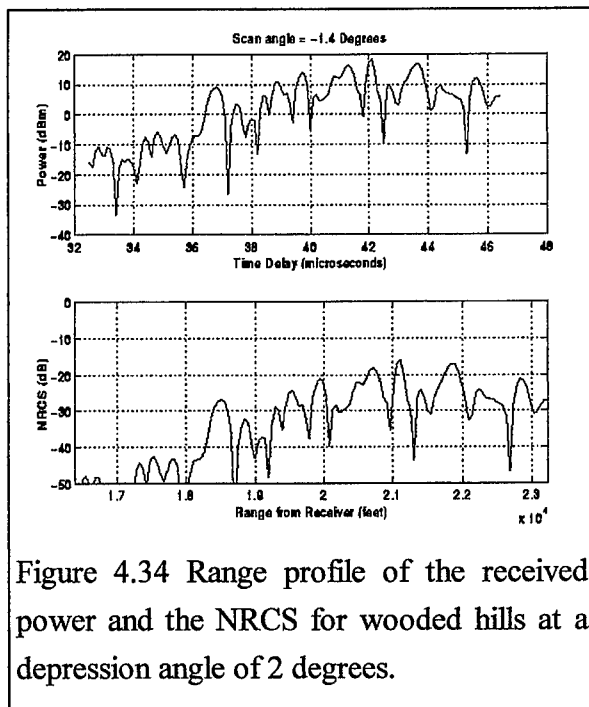
Figure 4.34 Range profile of the received power and the NRCS for wooded hills at a depression angle of 2 degrees.
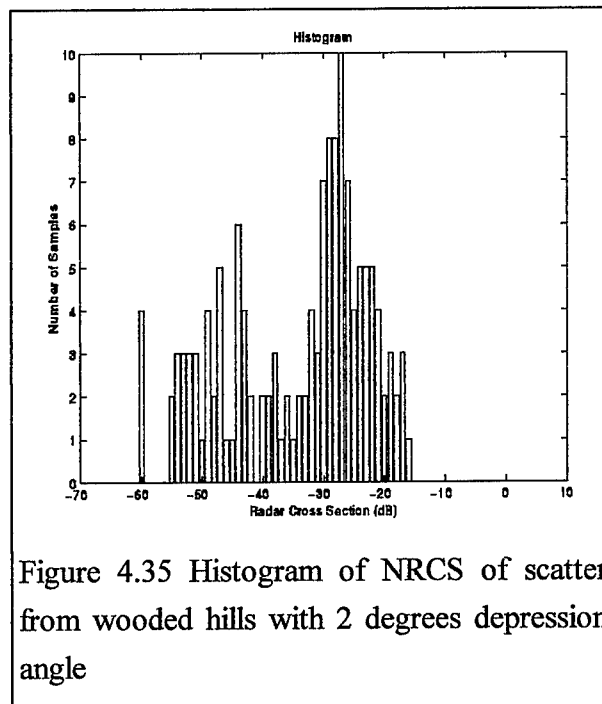
Figure 4.35 Histogram of NRCS of scatter from wooded hills with 2 degrees depression angle

4.3.3 Wooded Hills

The final measurement records the backscatter from the wooded hills located three to four nautical miles from the receiver. As shown in Figure 4.33, the backscatter power from these hills is associated with the trees and slopes northwest of the village of Newport.

Figure 4.34 shows that significant power is received from this region even though 4 nautical miles is close to the maximum usable range of the bistatic system using the local transmitter. The histogram in Figure 4.35 reflects the high mean amplitude as well as the increased spread associated with the lower depression angle of 2 degrees. The mean NRCS was measured as -25.8 dB with a median value of -30.0 dB.

Figure 4.33 Receiver power from the wooded hills north of the village of Newport

4.4 Calibration Procedures for Attenuation and Multipath Experiments

One way that the vegetation and terrain inhibit the detection and tracking of the desired targets is by providing strong signals that can mask the smaller target returns. Knowledge of this interference is required to estimate the performance of existing and candidate system. The previous section discussed the procedures for quantifying this interference using a calibrator.

Another way the vegetation and terrain can inhibit target detection is by the attenuation of the illuminating signal before it impinges on the target and/or by attenuating the signal reflected by the target. Furthermore, if this attenuation changes rapidly as a function of time, this fluctuation will also be modulating the target return and changing the detection statistics of the target. Measurements of this attenuation and multipath effect are needed to determine the successfulness of this screening and to determine the best system for mitigating these effects.

Toward this end, the calibrator can be used to provide a constant target of known value for the purpose of measuring these effects. The first step in this procedure is to measure the bistatic return from the calibrator when it is in a "clear" region that is directly visible to both the bistatic transmitter and receiver and has minimal multipath. Then the calibrator is moved into the vegetation and the calibrator bistatic signal is recorded to measure the mean and variance of the attenuation as a function of time and frequency. The auxiliary information recorded for each measurement should include the thickness of the vegetation screen, the density and type of vegetation, the amount of moisture present and the wind speed. The measurement should be repeated several times to develop a statistical measure of the attenuation.

The calibrator provides a high signal-to-noise signal that can measure two-way net attenuation levels exceeding 60 dB. Some of these measurements are being performed at the Newport site in 1998 as part of an investigation of the capability of S-band in detecting and tracking moving targets masked by vegetation. Figure 4.36 and Figure 4.37 show the measurements of the calibrator in the clear and screened by a thick hedge of trees, respectively. Without attenuation, the use of a 64 pulse burst and a LFM waveform with a BT product of over 100, the calibrator can provide a signal-to-noise ratio exceeding 80 dB at test ranges of 2 miles. Figure 4.36 shows an example (64 pulse burst, bandwidth=5 MHz, pulse width=40 usec, BT=200) where the processed signal power is 60.3 dBm. The display shows a time extent dominated by the range sidelobes that generally exceed 0 dBm. Beyond the sidelobe region, the thermal noise level is -40 dBm and the signal-to-noise ratio is approximately 100 dB.
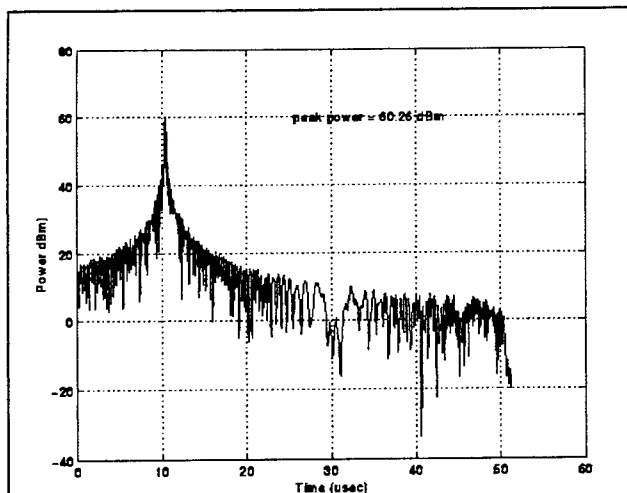
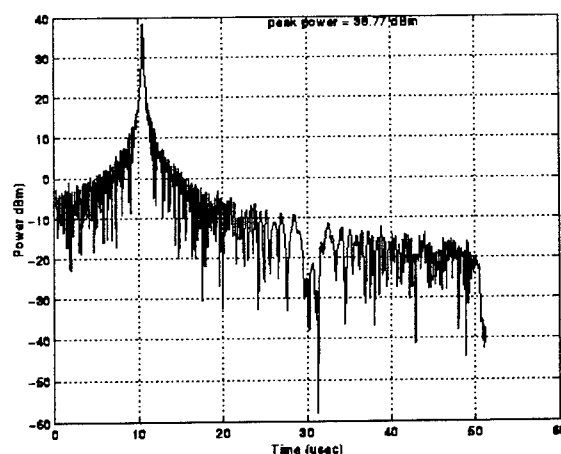Figure 4.36 Calibrator signal with no attenuation by local vegetation

Figure 4.37 Calibrator signal screened by the vegetation

Figure 4.37 shows the received power when the calibrator is screened by the vegetation both in the transmit path and the receiver path. The signal power is 38.8 dBm, representing a two-way net loss of 21.5 dB.

5.0 SUMMARY AND CONCLUSIONS

This report has presented the procedures for using the calibrated transponder with the bistatic receiver testbed for the purpose of performing clutter measurements. The report presented a description of how the calibrated transponder works and presented the equivalent radar cross section of the past and current transponder. Measurements performed in the field identified a site with minimal multipath and demonstrated a day-to-day procedure that resulted in a calibration accuracy of approximately +/- 1 dB.

The report also showed the limitations of a ground-based bistatic receiver in performing measurements due to mainbeam multipath, especially when the receiver is used in a look-down mode. A calibration constant was derived and demonstrated for performing calibrated measurements of point and distributed targets. The technique was used to perform measurements of several clutter sources and the results are summarized in Table 6 .1 for point targets and Table 6.2 for distributed targets.

To improve the ground truth associated with the measurements, the clutter returns were correlated with a topographic map after translation of the radar data from polar coordinates to maps rectangular coordinates. This approach can also be used to correlate the bistatic target returns with returns from monostatic radars in an adjunct bistatic receiver mode.

Finally, recommendations were presented for using the calibrated transponder to measure the attenuation of screened targets and to assist in the investigation of detecting moving targets screened by vegetation or terrain.

Table 6.1 System parameters in measurements of point targets

Target Description	Range from rec. (feet)	Depression angles Tx (deg)	Depression angles Rec. (deg)	Bistatic Angle (deg)	Number of pulses	Number of cells	Mean RCS (dBsm)	Median RCS (dBsm)
Town Barn	12215	4.5	4.0	5	16	45	11.1	6.7
Farm	4500	4.6	5.1	27	16	18	1.9	0.0
Village	16370	3.4	3.5	3	16	62	13.2	7.1

Table 6.2 System parameters of the distributed clutter measurements

Target Description	Distance From Recr (feet)	Depr. Angles Trans (deg)	Depr. Angles Recr (deg)	Bistatic Angle (deg)	Resoln Cells	Mean NRCS (dB)	Median NRCS (dB)
Forest	4497	8.0	7.8	36	7	-25.3	-27.0
Forest	6000	6.0	6.0	26	14	-22.4	-29.6
Forest	9840	4.0	3.7	11	30	-24.2	-26.2
Wooded Hills	18748	2.0	1.6	6	179	-25.8	-30.0
Golf Course	13438	3.4	2.4	13.6	87	-27.6	-32.4

6. BIBLIOGRAPHY

[1] Wang, H. and Cai, L., "On Adaptive Spatial-Temporal Processing or Airborne Surveillance Radar Systems", IEEE Transactions on Aerospace and Electronic Systems, AES-30, 3 (July 1994), 660-670.

[2] Barbarossa, S and Farina, A. "Space-Time-Frequency Processing of Synthetic Aperture Radar Signals,", IEEE Transactions on Aerospace and Electronic Systems, AES-30, 2 (April 1994), 341-358.

[3] Fante, R. L., "Cancellation of Specular and Diffuse Jammer Multipath Using a hybrid Adaptive Array", IEEE Transactions on Aerospace and Electronic Systems, AES-27, 5 (September 1991), 823-836.

[4] Morgan, D. R. and Aridgides, A., "Adaptive Sidelobe cancellation of Wide-Band Multipath Interference", IEEE Transactions Antennas and Propagation, AP-33, (August 1995), 908-917.

[5] Tang, C. E. T., Liu, K. J. R., and Tretter, S. A., "Optimal Weight Extraction for Adaptive Beamforming Using Systolic Arrays", IEEE Transactions on Aerospace and Electronic Systems, AES-30, 2 (April 1994), 367-384.

[6] Simkins, W. L., <u>Multichannel Receiver Characterization for Adaptive Array Applications, Phase 1: Characterization of the Bistatic Receiver Testbed,</u> Dec. 1995.

[7] Simkins, W. L., <u>Multichannel Receiver Characterization for Adaptive Array Applications, Phase 2: Algorithms for Calibration of the Bistatic Radar Testbed,</u> April, 1997.

[8] Private Communication with Mr. Thomas Scatko, RL/OCTM.

[9] Test and Measurement Catalog, Test and Measurement Sector, Hewlett-Packard, Santa Clara, CA, 1993.

[10] Skolnik, M. I., *Introduction to Radar Systems*, McGraw-Hill Book Company, New York, 1962.

[11] Scheer, J. A. and Kurtz, J. L. (editors), *Coherent Radar Performance Estimation*, Artech House, Boston, MA, 1993.

[12] Theory of Operations for AASR Receiver Subsystem, TSC-H601-PD-008, 20 July, 1989.

[13] HP E1429A/B, 20 MSa/s 2-Channel Digitizer, Users Manual, Hewlett Packard June, 1993.

[14] Kerr, Donald E., *Propagation of Short Radio Waves*, McGraw-Hill Book Company, Inc., New York, 1951.

[15] Bullington, K., "Radio Propagation Fundamentals,", *Bell System Technical Journal*, Vol. 36, no. 3, pp 593-626, 1957.

[16] Blake, L. V., A Guide to Basic Pulse-radar Maximum-Range Calculation Part 1-Equations, Definitions, and Aids to Calculations, NRL Report 6930, Dec. 1969, AD701321.

[17] Battan, L. J., *Radar Observation of the Atmosphere*, University of Chicago Press, Chicago, 1973.

[18] Simkins, W. L., FAA Clutter Model Upgrade, RADC-TR-90-170, October, 1990.

[19] Simkins, W. L., Clutter Analysis for ADI, RL-TR-95-31, March 1995.

[20] Currie, Nicholas, C., *Techniques of Radar Reflectivity Measurement*, Artech House, Inc, 1984.

[21] Phase IV Systems, Inc., 3405 Trianna Blvd, Huntsville, AL 35806-4695.

[22] Blake, L.V., Antenna and Receiving-System Noise-Temperature Calculations, NRL Report 5668, Sept. 1961, AD265414.

[23] Oppenhiem, A.V. and Schafer, R. W., *Digital Signal Processing*, Prentice-Hall, Englewood Cliffs, New Jersey, 1975.

[24] Papoulis, A., *Signal Analysis*, McGraw-Hill, New York, New York 1977.

[25] Rabiner, L. R., and Gold, B., *Theory and Application of Digital Signal Processing*, Prentice-Hall, Inc., 1975.

[26] Ho, K.C., Chan, Y. T., Inkol, R., "A Digital Quadrature Demodulation System," AES-32-4, October, 1996, 1218-1226.

[27] Rice, D. W. and Wu, K. H., " Quadrature Sampling with High Dynamic Range,", AES-18, (4 Nov 1982), 726-739.

[28] Ward, H. R., "An Optimum Filter for Direct A/D conversion," AES-27, 56 (Nov. 1991), 883-886.

[29] Rader, C. M., " A Simple Method for Sampling In-phase and Quadrature Components", AES-20, 6 (Nov 1984), 821-824.

[30] Mitchell, R. I., " Creating Complex Signal Samples from a Band-limited Real Signal", AES-25, 3 (May 1989(, 425-427.

[31] Willis, Nicolas J., *Bistatic Radar,* Technology Service Corporation, Artech House, Norwood, MA, 1991.

[32] Cook, C. E., and M. Bernfeld, *Radar Signals-An Introduction to Theory and Applications,* Academic Press, Inc. New York, March, 1967.

[33] Nathanson, F. E., *Radar Design Principles,* McGraw-Hill Book Company, 1969.

[34] Skolnik, M. I., *Introduction to Radar Systems,* McGraw-Hill Book Company, New York, 1962.

[35] Simkins, W. L., Multichannel Receiver Characterization for Adaptive Array Applications, Phase 3: Assessment of the Bistatic Receiver Testbed as a Measurements Tool for Clutter Phenonmenology, AFRL-SN-RS-TR-1998-44, April 1998.

[36] Barton, D. K. and Ward, H. R., *Handbook of Radar Measurement,* Artech House, Inc., 1984.

[37] Way, J.B. et al, " Diurnal Change in Trees as Observed by Optical and Microwave Sensors: The EOS Synergism Study", GE-29-6, pp 807-821, 1991.

[38] Carlson, A. B., *Communcation Systems: An Introduction to Signals and Noise in Electrical Communication,* McGraw-Hill Book Company, New York, 1968.

[39] Simkins, W. L., Multichannel Receiver Characterization for Adaptive Array Applications, Phase 2: Algorithms for Calibraiton fo the Bistatic Receiver Testbed, (unpublished draft) April 8, 1997.

[40] Photographs provided by Ms. Elaine Kordyban, AFRL/SN.

Appendix A. Terms and Definitions

$A_e(\theta, \phi)$ = Receive antenna aperture toward elevation ϕ and azimuth θ (meter^2)

A_{col} = effective aperture of a column array

A_{row} = effective aperture of the row dimension created by digital beamforming

B_{coh} = noise bandwidth of a coherent processing interval $\cong \dfrac{L_{wtr_n} B_s}{n_{beam}}$ (Hz)

B_n = noise bandwidth of analog receiver (Hz)

B_s = bandwidth of signal $\leq B_n$ (Hz)

DC = duty cycle = $\dfrac{\tau_u}{T_{pri}}$

$F_t^2(\theta, \phi)$ = transmit propagation pattern

$F_r^2(\theta, \phi)$ = receiver propagation pattern

G_{pc} = pulse compression S / N gain = $\dfrac{L_{wtr\,s}}{L_{wtr_n}} B_s \tau_u \approx \dfrac{\tau_u}{\tau_c}$

G_r = Receiver amplication

$G_t(\theta, \phi)$ = Transmit gain at azimuth θ and elevation ϕ relative to the maximum gain at $G_t(0,0)$

L_{wta} = weighting loss in azimuth beamforming

L_e = environment losses

L_{col} = loss within a column array

L_{comp_s} = signal loss in compensation network

L_{comp} = signal - to - noise loss in compensation network

L_p = signal processing losses

L_r = receiver losses

L_t = transmit losses

$L_{wta\,n}$ = noise loss of azimuth beamforming weighting

L_{wta_s} = signal loss of azimuth beamforming weighting

L_{wta} = signal - to - noise loss of azimuth beamforming weighting

$L_{wtp\,n}$ = noise loss of Doppler filter weighting

L_{wtp_s} = signal loss of Doppler filter weighting

L_{wtp} = signal - to - noise loss of Doppler filter weighting

$L_{wtr\,n}$ = noise loss of pulse compression weighting

$L_{wtr\,s}$ = signal loss of pulse compression weighting

L_{wtr} = signal - to - noise loss of pulse compression weighting

n_{beam} = number of pulses per beam

N_{col} = number of columns

N_p = number of pulses coherently integrated

P_t = Transmitter Peak Power = Average power within the pulse (watts)

$\bar{P}_t$ = average transmit power = (DC) P_t (watts)

ρ = match filter response to a single pulse

R_r = Range from the receiver to the target (meters)

R_t = Range from the transmitter to the target (meters)

S = average signal power within the pulse

$S(\omega)$ = signal voltage spectrum (italics used to distinguish from signal power)

T_{beam} = observation time per beam = $n_{beam} T_{pri}$ (seconds)

$T_s(\theta, \phi)$ = System noise temperature in elevation ϕ and azimuth θ (°K)

T_{pri} = pulse repetition interval (sec)

$T_{sc} = \dfrac{T_{beam}\Psi}{\Omega}$ = time to scan solid angle Ψ (sec)

$u(t)$ = transmit waveform

$\chi(\tau, \omega_d) = \left. \displaystyle\int_{-\infty}^{\infty} u(x)u^*(\tau+x)e^{j\omega_d x}\, dx \middle/ \chi_n \right.$ = normalized ambiguity function of the burst waveform

where τ and ω_d are offsets from the peak of the burst matched filter response.

$\chi_n = \displaystyle\int_{-\infty}^{\infty} n(x)u^*(\tau+x)e^{j\omega_d x}\, dx$ = burst matched filter response to noise

ϕ = elevation angle

θ = azimuth angle

η_a = antenna efficiency (uniform weighting)

κ = Boltzmann's constant = $1.38*10^{-23}$ watt − second / °K

$\sigma_t(\beta, \varphi, \gamma)$ = Target RCS at bistatic angle β and aspect (φ, γ) (meter^2)

τ_u = uncompressed pulsewidth (sec)

τ_c = compressed pulsewidth (sec)

Ω_t = solid angle of transmit beam (steradians)

Ψ_t = solid angle to be searched by transmitter (steradians)